Politécnica UFRJ

COMPUTATIONAL MODELING OF THE HOMOGENEOUS CONDENSATION PHENOMENON APPLIED TO SUPERSONIC SEPARATORS

Pedro Kropf de Azevedo

Undergraduate Project presented to the Mechanical Engineering course of POLI/UFRJ as partial fulfillment of the requirements for the degree of Mechanical Engineer.

Advisors: Gustavo Rabello dos Anjos
Tânia Suaiden Klein

Rio de Janeiro
Outubro de 2022

UNIVERSIDADE FEDERAL DO RIO DE JANEIRO

Mechanical Engineering Department

DEM/POLI/UFRJ

COMPUTATIONAL MODELING OF THE HOMOGENEOUS CONDENSATION PHENOMENON APPLIED TO SUPERSONIC SEPARATORS

Pedro Kropf de Azevedo

FINAL UNDERGRADUATE PROJECT SUBMITTED TO THE TEACHING STAFF OF THE MECHANICAL ENGINEERING DEPARTMENT FROM POLI/UFRJ AS PARTIAL FULFILLMENT OF THE REQUIREMENTS FOR THE DEGREE OF MECHANICAL ENGINEER.

Approved by:

Prof. Gustavo Rabello dos Anjos, Ph.D.

Profa. Tânia Suaiden Klein, Ph.D.

Antonio de O. Samel Moraes, D.Sc.

Prof. Roney Leon Thompson, Ph.D.

Marcelo da Costa Amaral, M.Sc.

RIO DE JANEIRO, RJ – BRAZIL

OCTOBER 2022

Kropf de Azevedo, Pedro

Computational Modeling of the Homogeneous Condensation Phenomenon Applied to Supersonic Separators/ Pedro Kropf de Azevedo. – Rio de Janeiro: UFRJ/Escola Politécnica, 2022.

XV, 56 p.: il.; 29, 7cm.

Advisors: Gustavo Rabello dos Anjos

Tânia Suaiden Klein

Undergraduate Project – UFRJ/ POLI/ - Mechanical Engineering Course, 2022.

Bibliographic references: p. 58 – 61.

1. Supersonic Flow. 2. Fluid Mechanics. 3. OpenFOAM. 4. Homogeneous Condensation. 5. Compressible Flow. 6. Computational Fluid Dynamics. I. Rabello dos Anjos, Gustavo *et al.*. II. Universidade Federal do Rio de Janeiro, UFRJ, Mechanical Engineering Course. III. Computational Modeling of the Homogeneous Condensation Phenomenon Applied to Supersonic Separators.

To my grandfather Tonho, who was my inspiration to become a mechanical engineer.

Thanks

I would like to first thank my family. My parents, Luciana and Danillo, who have always provided me with all the necessary conditions to have access to education and healthcare, in addition to motivating and supporting me in my decision to pursue mechanical engineering. My brother João, who has always been by my side in good and bad times and has never let me down. Thank you so much for always being there for me. My grandfather, Luiz Antônio, who unfortunately could not witness the realization of my dream of studying mechanical engineering at UFRJ, thank you for inspiring me to follow the same path you did; if I graduate as an engineer today, it is largely thanks to you. I know that in some way, you are accompanying me and participating in these achievements.

I would like to thank all my friends that college brought me, especially my coursemates affectionately nicknamed MECrias. I want to mention the names of each member, one by one: Bellini, Breno "Chocolate", Dudu, Freitas, Ribeiro and Ribeiro "Barba", Francês, Bari, Bia "Gates", Spesani, João, Nunes, Limão, "Fluffy", Paulo, Renan, Rômulo, Silveira and Yan. Thank you so much for the unforgettable moments, parties, and study groups. With you by my side, college became much more enjoyable and fun. I take our friendship for life.

A special thanks to the faculty of the mechanical engineering department for their high professionalism and also for all the knowledge they imparted to the students in a formidable way. Thank you to all the staff of UFRJ for taking care of this heritage and providing great study infrastructure for the students.

Finally, I would like to thank the colleagues and friends I made at WIKKI Brasil, the company that welcomed me very early in college and played a fundamental role in my personal and engineering development. Rodrigo, Robson, Paulo, Lange, Samel, and Jovani, thank you so much for giving me the opportunity to learn and grow with you. To my advisors, Prof. Gustavo Rabello, Prof. Tânia Klein, and Samel thank you very much for your patience, guidance, and also for the honor of having my work advised by professionals like you.

Abstract of Undergraduate Project presented to POLI/UFRJ as partial fulfillment of the requirements for the degree of Mechanical Engineer.

COMPUTATIONAL MODELING OF THE HOMOGENEOUS CONDENSATION PHENOMENON APPLIED TO SUPERSONIC SEPARATORS

Pedro Kropf de Azevedo

October/2022

Advisors: Gustavo Rabello dos Anjos
Tânia Suaiden Klein

Departament: Mechanical Engineering

This study addresses a proposal for mathematical modeling of the homogeneous condensation phenomenon that occurs in supersonic separators. Such equipment aims to separate contaminants in gas mixtures, such as the exploration of natural gas in pre-salt reservoirs. In this scenario, the separation of carbon dioxide, present as a contaminant of methane gas, is of great economic and environmental interest. Computational simulation is an important tool to make the construction of more efficient equipment possible, where the condensation of the contaminant and its removal can be improved. Therefore, this work reviews the current mathematical models for the phenomenon of homogeneous condensation and proposes its implementation in a compressible flow solver using the OpenFOAM framework. This solver is firstly validated against experimental data available in the literature to be used in an initial analysis of a new design of a supersonic separator.

Resumo do Projeto de Graduação apresentado à Escola Politécnica/UFRJ como parte dos requisitos para obtenção do título de Engenheiro Mecânico.

MODELAGEM COMPUTACIONAL DO FENÔMENO DA CONDENSAÇÃO HOMOGÊNEA APLICADA A SEPARADORES SUPERSÔNICOS

Pedro Kropf de Azevedo

October/2022

Advisors: Gustavo Rabello dos Anjos
Tânia Suaiden Klein

Departmento: Engenharia Mecânica

O presente estudo aborda uma proposta de modelagem matemática para o fenômeno da condensação homogênea que ocorre em separadores supersônicos. Tais equipamentos visam realizar a separação de contaminantes em misturas gasosas, como é o caso da exploração de gás natural em reservatórios do pré-sal. Neste cenário, a separação do gás carbônico, presente como contaminante do gás metano, é de grande interesse econômico e ambiental. A simulação computacional é uma importante ferramenta para viabilizar a construção de equipamentos mais eficientes, onde a condensação do contaminante e sua remoção sejam as maiores possíveis. Portanto, o presente trabalho apresenta uma revisão dos atuais modelos matemáticos para o fenômeno, implementação em um solver OpenFOAM, validação contra dados experimentaise resultados iniciais do escoamento de misturas gasosas em um separador supersônico.

Contents

List of Figures

List of Tables

List of Symbols

Pr	Prandtl Number, p. 18
S	Supersaturation degree, p. 14
$\boldsymbol{S}$	Surface area magnitude vector, p. 6
$\boldsymbol{U}$	Velocity vector, p. 6
$\boldsymbol{g}$	Gravity, p. 6
κ	Gas thermal conductivity, p. 18
ν_t	Turbulent viscosity , p. 19
ρ	Density, p. 6
ρ_g	Gas Density, p. 12
ρ_l	Liquid Density, p. 12
σ	Surface tension, p. 14
a	Speed of sound , p. 5
e	Internal energy, p. 6
r	Droplet radius, p. 14
rc	Droplet critical radius, p. 14
x^*	Distance from throat, p. 33
M	Mach Number, p. 5
R	Gas constant, p. 6
T	Temperature, p. 6

h	Enthalpy, p. 6
p	Static pressure, p. 6

List of Abbreviations

A.R	Aspect Ratio, p. 28
DPE	Discrete Phase Model, p. 9
R.D	Relative difference, p. 38

Chapter 1

Introduction

The present work aims to study, implement and validate mathematical modeling for the homogeneous condensation of contaminant components of multiphase gaseous mixtures in supersonic separators.

There are several processes in the industry that requires the separation of certain components of gaseous mixtures, mainly in the natural gas stemming from the petroleum reservoirs, for example, the exploration of pre-salt rocky formations. In this last process, the presence of water vapor, heavy hydrocarbons, and carbon dioxide in the mixture could cause a series of problems in the exploration and distribution chain, such as the mixture's specific heat reduction, corrosion, hydrate formation, pipeline blockage, and carbon dioxide emission [4]. In this scenario, the separation of those contaminants from the methane gas is of the utmost importance from an economic and environmental perspective. Among the conventional methods of separation, the use of membranes, absorption, adsorption, and cryogenic stand out.

Supersonic separators work as an alternative to conventional means of separation because of their compact proposal and geometrical simplicity. The structure of a supersonic separator is composed of a convergent-divergent channel, where the flow evolves from subsonic to supersonic velocities. The position where the flow becomes supersonic is called "throat", which has a smallest cross sectional area in the equipment. The pressure and temperature conditions reached right after the "throat" by the gaseous mixture would make the contaminant condense. A strong rotational field is imposed and, due to the density difference between gas and liquid phases and the rotational movement of the fluid, the droplets formed in the condensation process are directed to the walls of the supersonic separator and are collected in side outlets, while the "clean gas" leaves the equipment at the end of the divergent section [5].

Thus, the capacity to predict the efficiency of the condensation inside the equipment and control the contaminant's droplets capture is fundamental to the development of an optimized supersonic separator, which depends on accurate modeling of the homogeneous condensation phenomenon. In this way, computational fluid dynamics is an important tool in the design of optimized equipment, given the scarcity of experimental data and consistent modeling in the literature.

1.1 Objectives

The main objectives of this work are:

- To study the most recent developments and models in the subject;
- Validation of the homogeneous condensation model implemented in a compressible multicomponent flow solver in the OpenFOAM;
- To understand the condensation phenomenon and its behavior inside a new design of a supersonic separator.

To achieve this, several works were reviewed and here documented in a way that the modeling of the homogeneous condensation of gases could be done with the latest developments available in the literature. Besides that, a review of different approaches to the problem was made so that the most convenient path to implement the mathematical models could be chosen.

Chapter 2

Bibliography Review

This chapter conducts a bibliography review about supersonic separators and their applications, multi-phase flows, and homogeneous condensation phenomenon, passing through several authors, models, and possible approaches for solving the problem aiming for a robust and precise way of modeling the homogeneous condensation in gaseous mixtures. Thus, the reader will be aware of the numerous ways of approaching the problem and the analysis process applied in this work to choose the model that best fits this application.

2.1 Supersonic Separators and Its Applications

Supersonic separators are equipment designed to separate gaseous mixtures with an imposition of a strong centrifugal field (which can reach around 500000 times the gravity force) on the flow. This effect is achieved, for example, by the positioning of fixed vanes in the entering section of the equipment, making the fluid rotate. Its geometry consists of a convergent channel where the flow is subsonic, followed by a reduction in the cross-sectional area called "throat", where the flow becomes sonic, and then a divergent section where the flow becomes supersonic. With so, an ideal thermodynamic state is desired for the homogeneous condensation of a specific component of the mixture, creating condensed droplets that follow the gas current. Due to the density difference between the gas and liquid phases and the centrifugal field, the droplets are directed to the separator's walls forming a liquid film.

At the end of the separation, the fluid goes through the diffusor - the divergent region of the equipment - where all the liquid generated is collected by gaps near the walls; the "clean" gas remains positioned majority at the center of the equipment and follows the

divergent region, causing an increase in the pressure (pressure recuperation) at the outlet. A peculiarity of this type of separation is the shock wave produced right after the throat of the equipment (region of greatest area constriction), due to the very high velocities achieved - Mach numbers above 2.0 are easily obtained. This phenomenon results in an increase of temperature and pressure, creating the conditions for condensation to happen. The equipment's efficiency is intrinsically connected to its capacity of generating shock waves and their positioning because that is the region where the thermodynamic conditions are ideal for homogeneous condensation to happen.

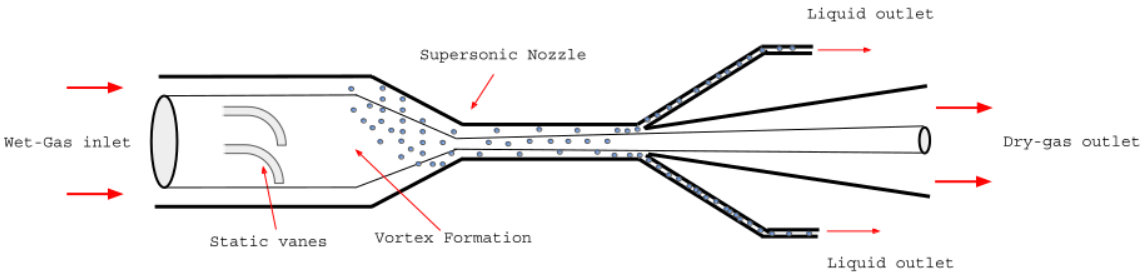

Figure 2.1: Supersonic Separator Scheme.

The first supersonic separator was proposed at the end of the 60s, but didn't have much success, since it had difficulties performing in operational conditions. However, in the mid-90s modern proposals arrived in the industry: developed separately by two groups, the Twister BV, and the Translang Technologies Ltd. was the most notable [6] [7].

The first model cited was developed for dehydration and conditioning of the natural gas and recuperation of heavy hydrocarbons, according to [8]. After improvements in the project, such as the addition of fixed vanes in the inlet, and the introduction of an internal tube, the new model presented a removal efficiency of 90% of the condensable products with a pressure loss of 25% [9].

About the Translang Technologies Ltd., proposed by Russian researchers, has a very similar geometry to the previous one with a constant inlet section with static vanes that impose a rotational field in the flow; after that, the fluid passes through a convergent region where the flow is accelerated to supersonic velocities, condensing part of the mixture components. Finally, the condensed droplets are collected near the diffusor, where the gas has its pressure recovered and is collected [10].

With that said, supersonic separators are novel technologies utilized to separate gaseous mixtures. Its applications are extensive, but in the Oil and Gas industry context it can be applied in the natural gas production lines. The separation of Methane

from contaminants such as Carbon Dioxide by compact and low-cost production equipment can be very interesting, turning the optimization of the geometry and the study of the intrinsic physical phenomena into a process of great importance.

2.2 Compressible Flows

Defining some variables and the behavior of compressible flows is crucial to the analysis presented in this work. Consequently, this section is focused on the review of relations for compressible flows considering the formation of shock waves. The following hypothesis were considered:

- Inviscid Flow
- Perfect Gas

Neglecting the viscosity of the fluid in the formulation is a plausible hypothesis for the bulk region of the flow, considering the high Reynolds number, which indicates that the advective forces are way higher than the viscous forces. Thus, the qualitative interpretations of the formulations here derived will not be influenced by the viscosity of the fluid. However, the final mathematical model will consider the viscosity as the turbulent regime plays an important role in the behavior of the flow inside the supersonic separator. Besides, the turbulent mathematical modeling only applies to viscous fluids.

The most convenient way to measure if a gas flow can be considered incompressible, or whether it must be treated as compressible, is the Mach number M, , defined as the ratio between the gas flow velocity U and the speed of sound in the considered medium, a :

$$M = \frac{U}{a} \, , \tag{2.1}$$

and it depends on the location where it's measured, so this is the local Mach number. It is largely accepted that, for the low-speed flow of gases (under Mach 0.3), the associated pressure changes are small, so the flow can be considered incompressible. However, the main objective of this work is the application in supersonic separators, which indicates that the main flow regime studied will be supersonic, with $M > 1$. This implies that we shall deal with shock waves, non-isentropic processes, and a series of particularities that comes with the supersonic regime.

For compressible flows, the density ρ of the fluid is variable and becomes unknown. Hence, an additional governing equation to the conservation of mass and momentum is needed: the energy equation; which introduces the internal energy e as an unknown. Since the internal energy is related to the temperature T , this one becomes another important variable in our system. Finally, we have five important variables to solve for: $p, \boldsymbol{U}, \rho, e$, and T . To do so, we need five governing equations as well, described in their differential forms below for inviscid flows. The process of derivation of the continuity 2.2, momentum 2.3, and energy 2.4 equations can be found at [11]:

$$\frac{\partial \rho}{\partial t} + \nabla \cdot (\rho \mathbf{U}) = 0 \, , \tag{2.2}$$

$$\rho \frac{D\mathbf{U}}{Dt} = -\nabla p + \rho \mathbf{g} \, , \tag{2.3}$$

$$\rho \frac{D(e + \mathbf{U}^2/2)}{Dt} = -\nabla \cdot \Big(p\mathbf{U}\Big) + \rho(\mathbf{g} \cdot \mathbf{U}) \, , \tag{2.4}$$

$$h = e + \frac{p}{\rho} \, . \tag{2.5}$$

The three equations above constitute the so-called Euler equations and solve for three of our five unknowns. Assuming a calorically perfect gas, the last two equations to complete our system are the equation of state 2.6 and the internal energy equation 2.7:

$$p = \rho R T \, , \tag{2.6}$$

$$e(T) = e_{ref} + \int_{T_{ref}}^{T} c_v(T) dT \, . \tag{2.7}$$

These equations close our system of a compressible, adiabatic, and calorically perfect gas. But these equations are no longer valid when it comes to a scenario with shock waves, which is a region where a non-isentropic process takes place and the flow properties change drastically. There are special formulations using the Mach number and stagnation properties that allow us to calculate the properties downstream of the shock wave. Figure 2.2 shows a schematic of a normal shock wave:

Considering the system aforementioned (steady-state, compressible, adiabatic, no viscous effects, and no body forces), applying the integral form of the conservation equations to the control volume defined above:

$$\oint_S \rho \boldsymbol{U} \cdot \, d\boldsymbol{S} = 0 \, , \tag{2.8}$$

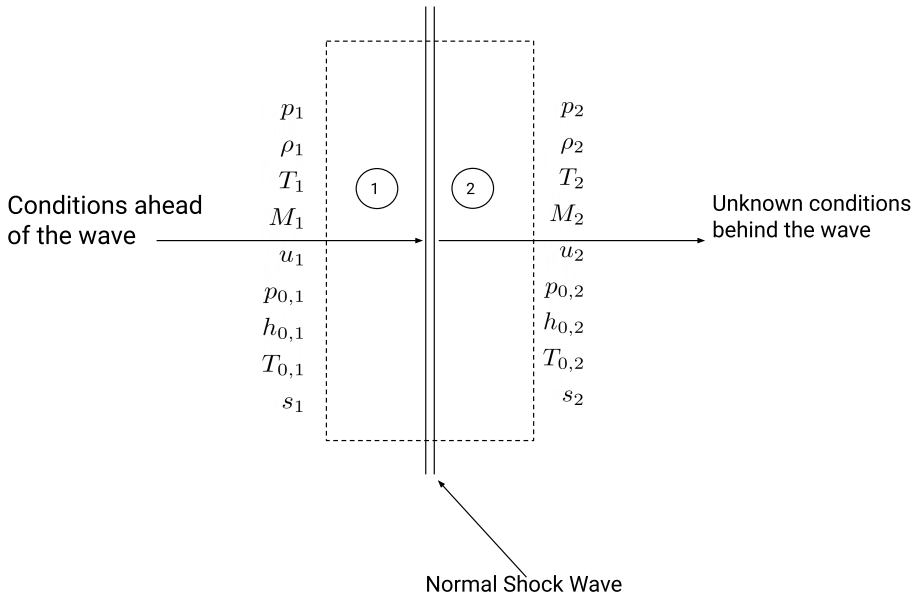

Figure 2.2: Schematic representation of a shock wave.

$$\oint_S (\rho \boldsymbol{U} \cdot \ dS)\ \boldsymbol{U} = -\oint_S p d\boldsymbol{S}\ , \tag{2.9}$$

$$\oint_S \rho \left(e\ +\ \frac{U^2}{2} \right) \boldsymbol{U} \cdot d\boldsymbol{S} = -\oint_S p \boldsymbol{U} \cdot d\boldsymbol{S}\ , \tag{2.10}$$

where Equations 2.8, 2.9 and 2.10 are the integral forms of the mass, momentum, and energy equations for the control volume above with surface S. Evaluating these integrals over the surface, the Equations above become 2.11, 2.12, and 2.13:

$$-\rho_1 u_1 A_1 + \rho_2 u_2 A_2 = 0\ , \tag{2.11}$$

$$p_1 + \rho_1 u_1^2 = p_2 + \rho_2 u_2^2\ , \tag{2.12}$$

$$h_1 + \frac{u_1^2}{2} = h_2 + \frac{u_2^2}{2}\ . \tag{2.13}$$

The energy equation can be written as a function of enthalpy by its definition: $h \equiv e + pv$. Besides, we can add to the system two more equations, as done before: one equation of state and the enthalpy equation for calorically perfect gases:

$$h_2 = c_p T_2\ , \tag{2.14}$$

$$p_2 = \rho_2 R T_2\ . \tag{2.15}$$

Special forms of the energy equations are also discussed in [11], which contributes to the analysis of properties in the presence of shock waves. Some other important relations to explicit here are the total conditions related to the static conditions. Since the speed of

sound in a ideal gas a is given by $a = \sqrt{\gamma RT}$, it is possible to express the temperature 2.16, pressure 2.17 and specific mass 2.18 as:

$$\frac{T_0}{T} = 1 + \frac{\gamma - 1}{2} M^2 \,, \tag{2.16}$$

$$\frac{p_0}{p} = \left(1 + \frac{\gamma - 1}{2} M^2\right)^{\gamma/\gamma - 1} \,, \tag{2.17}$$

$$\frac{\rho_0}{\rho} = \left(1 + \frac{\gamma - 1}{2} M^2\right)^{1/\gamma - 1} \,. \tag{2.18}$$

These ratios are functions of the local Mach only. For air ($\gamma = 1.4$), the results for these functions are all tabulated.

2.3 Multi-phase Flow

A multi-phase flow is composed of two or more phases where a phase can be described as a homogeneous portion of the system that has uniform physical and chemical characteristics. This type of flow can be easily found in nature when you consider for example the particles in suspension in the seawater. Moreover, in industrial processes as in the separation of petroleum phases, it is common to observe the existence of multi-phase flows.

In relation to the present phases in the flow, it's possible to classify them as dispersed or continuous. The dispersed phase is formed by discrete elements which are not connected between them. On the other hand, the continuous phase could be interpreted as a part of the system that fills a continuous and connected region. The Bubble flow in a liquid medium is a fine example of this system: the bubbles form the dispersed phase while the liquid is the continuous one.

It will be possible to observe the presence of an initial multi-component continuous phase (gas mixture) and, after the condensation phenomenon, the presence of a dispersed phase (droplets of CO2) in the continuous one (non-condensed fraction of the gas) in the system studied in this work. Thereby, a gas-liquid mixture is expected. According to [12], two-phase flows can be classified by the interface geometry following three principal classes: separated flows, transitional or mixtures, and dispersed flow. Each class has its own unique properties, where their definition is an object of great interest for a real characterization of the flow. Figure 2.3 below shows some examples of two-phase flow patterns:

Thus, it's important to define an approach method for this problem considering the characteristics of the flow. There are two important methods in the literature: Euler-

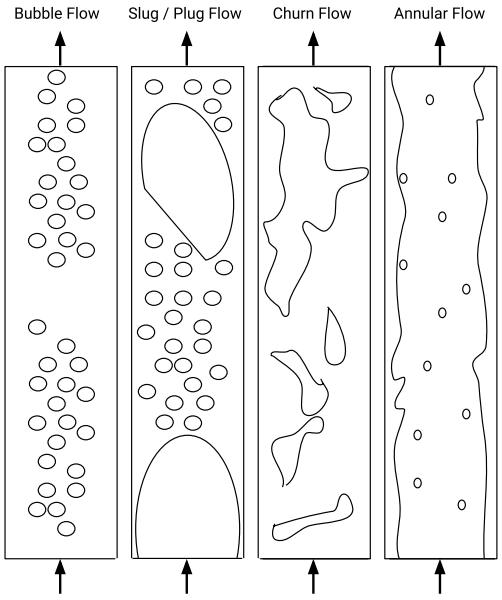

Figure 2.3: Examples of two-phase flow patterns in vertical pipes

Euler and Euler-Lagrange approaches. In the Euler-Euler approach, the phases are interpenetrating and treated as a continuum, being represented by phase-averaged conservation equations. On the other hand, the Euler-Lagrange model (also defined as Discrete Phase Model), represents the dispersed phase by individual DPEs , which are tracked through the flow domain by solving an appropriate equation of motion. The equations of motion of the dispersed phase are expressed in the Lagrangian formulation, while the continuous phase is expressed in the Eulerian frame. Figure 2.4 shows a visual representation of the differences between the models

Tracking the droplet particles generated by the condensation process and their path along the supersonic separator is not the main objective of this study. Despite the difficulty to develop a methodological strategy for lagrangian particle nucleation from an Eulerian phase, the computational effort is enormous due to the size and the number of generated particles. In that way, the Eulerian approach was chosen by being considered the most viable option for the phenomenon modeling. In the next sections, the Multi-Fluid Model and the Mixture Model will be presented, showing their advantages and disadvantages. This discussion is important to define the model to be used in this study.

2.3.1 Multi-Fluid Model

According to [13], the multi-fluid approach is widely used in applications involving transient phenomena, wave propagation, and change in flow patterns. In other words,

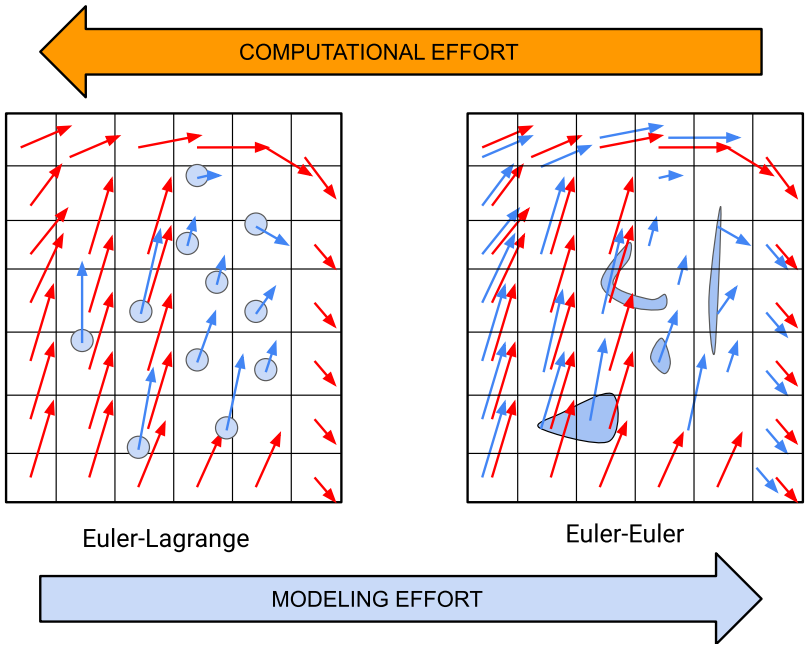

Figure 2.4: Euler-Euler x Euler-Lagrange Methods. Illustration based on [1]

scenarios where the phase coupling is considered weak (the inertia of one phase can change rapidly) are known to have a good response from the model. The transport equations are expressed separately for each phase in the system i.e, in a system with n-phases, there will be $2n$ coupled equations. Moreover, the phase interactions have to be modeled by means of closure equations.

An average process is employed in this kind of analysis, because of the random movements of the phases interfaces. In addition, solving instantaneous and local equations requires great computational resources. As an alternative, obtaining the average equations from the occurrence of one phase [13]. As the scope of this chapter is present the Multi-Fluid Model and its applications, the entire average process will not be discussed. For more information, refer to [13], [14] or [12].

One of the most discussed aspects of the Multi-Fluid Model is the need for closure equations to allow its solution. Even the monophase flow requires specifications of equations of state and constitutive equations to the viscous and Reynolds stress tensors. In the two-phase flow, we have additionally the constitutive relations for the phase interactions, which increases the complexity of the system. As [13] affirms, when the phases are "relatively decoupled", the model gives good results; when it's not the case, the model described in the next section is more indicated.

2.3.2 Mixture Model

The Mixture theory treats the macroscopic interactions of particles, where a great attraction of this formulation is that the mixture can be treated as a homogeneous fluid [13]. Unlike the Multi-Fluid Model, which consists of the most detailed and precise formulation for multi-phase flows, there are some intrinsic assumptions in the mixture model that turns it into a simpler, but still precise and robust model for types of flows where the phases are highly coupled.

One of the main differences between the models presented is the treatment of phases. In the mixture model, the n phases are treated as one, with specific rheological properties. In addition, the model does not consider one equation for each phase; as said before, it treats the phase mixture as one single fluid. Consequently, our equation system is reduced to one equation of mass, momentum, and energy. If the system has only two phases, we must have only one phase fraction transport equation.

The phase interaction is expressed by a diffusion model based on the relative movement between the phase and the velocity of the mass center of the mixture [13]. For a more detailed explanation and consultation, refer to [15]. In various references, the Mixture model is also called the Drift-Flux model because the diffusion velocity is expressed as the drift velocity, as shown in [12]. The drift velocity corresponds to the phase velocity relative to the center of the volume of the mixture.

The application of this model is generally accepted where the dynamics of the components of the mixture are closely coupled. However, applications, where the thermodynamic properties of each phase play a very important role in the system dynamics, could raise some questions and doubts about the reliability of the model. Besides it can introduce some difficulties in the numerical solution process.

2.3.3 Source-Term Model

Another formulation used by several authors consists of the source-term model [16], [**?**]. In this approach, the liquid phase formed by the condensation and the latent heat released in the process are represented by source terms in the mass, momentum, and energy equations, in addition to two more transport equations: the number of particles per unit volume formed in the condensation and the liquid mass fraction. Thus, a single-phase flow is considered but with two components: an inert and a condensable component. With an equation of state, the system is closed and one can solve the coupled pressure-velocity-energy equations. The mathematical formulation of this model will be discussed

in chapter 3.

In general, the source-term model has the advantage that the liquid fraction does not directly interfere with the thermodynamic calculations of the gas flow since the latent heat released is considered to be fully absorbed by the gaseous phase immediately. Finally, this type of modeling usually assumes that the droplet distribution can be properly represented by an equivalent mono-dispersion of average size; in other words, the average radius of the droplet is calculated by equation 2.19:

$$\overline{r_d} = \left(\frac{3\rho_g}{4\pi\rho_l} \frac{W}{(1-W)N} \right)^{1/3}, \tag{2.19}$$

where ρ_l and ρ_g stands for the liquid and gas densities respectively, W is the liquid mass fraction and N is the number of droplets generated. As the literature shows, the source-term model is able to predict with good agreement several experimental results. Besides that, the level of complexity in the solution of this model is lower when compared to the multi-fluid and mixture models. In this study, this model will be adopted and validated against experimental results obtained in the literature.

2.4 Homogeneous Condensation

Understanding the condensation of a vapor and its mechanisms is central to understanding the behavior of a wet-steam flow. Depending on the size distribution of droplets formed after the nucleation process, the flow behavior is completely affected. The process studied in this work, homogeneous condensation, can be described as the state path of a pure expanding vapor when it crosses the saturation line becoming supersaturated (the vapor does not condense immediately). A supersaturated vapor is in a meta-stable state for a period of time, which can vary depending on the degree of supersaturation. It reverses to an equilibrium state with the formation of vast and extremely small liquid droplets. On the other hand, heterogeneous nucleation refers to the condensation of any foreign particles present in the system but is not the main object of study here. With that said, a review of the classical nucleation theory, thermodynamic aspects, and novel methods will be discussed in this chapter.

2.4.1 Nucleation Theory

There are two main lines developed in the literature about homogeneous nucleation: the classical thermodynamic-kinetic approach, associated with BECKER [17],

MCDONALD[18], ABRAHAM [19], and a statistical mechanic-based one, created with the desire to eradicate uncertainties in the classical theory, although it has been always controversial, as reviewed in BAKHTAR [2]. Unfortunately, there is no definitive theory of nucleation in the literature.

However, many authors have studied and compared the results of the classical theory with experimental data. Laboratory studies with converging-diverging nozzles were made to observe nucleation and droplet growth in wet-steams flows. The measurement of center-line pressure distribution was the only data available from those experiments, which were used to deduce the limiting supersaturation [2]. Unfortunately, these results were insufficient to solve all the uncertainties involved in the nucleation phenomenon; in the 1960s and 1970s optical technologies were developed to measure the droplet size with certain precision, which provided additional data to the comparisons.

Bakhtar [2] says that the general conclusion of his work is that qualitatively the classical theory describes nucleation in steam nozzles well but quantitatively the predictive capability needs some improvements. With that said, the classical Becker-Döring theory is still the most used for engineering calculations.

2.4.2 Thermodynamic Characteristics

Some thermodynamic aspects of homogeneous nucleation will be discussed in this section following Bakhtar's work [2]. Forming a single spherical droplet with radius r from a supersaturated vapor held at constant pressure p and temperature T_g requires a reversible work defined by the change in the free Gibbs energy ΔG. If the vapor behaves as a perfect gas, the classical expression for ΔG is represented by Equation 2.20:

$$\Delta G = 4\pi r^2 \sigma - \frac{4}{3}\pi r^3 \rho_l R T_g \ln(S) \ , \tag{2.20}$$

where σ is the liquid surface tension coefficient, ρ_l is the liquid density and R is the gas constant. S is the supersaturation ratio defined by Equation 2.21

$$S = \frac{p_v}{p_s(T_g)} \ , \tag{2.21}$$

where p_v is the vapor pressure and $p_s(T_g)$ is the saturation pressure at T_g. A supersaturated vapor has $S > 1$ and the second right-hand term in Equation 2.20 is negative, while the first term is always positive. This term also dominates in most cases too as shown in Figure 2.5, while for a given value of supersaturation, ΔG increases with the radius r to a maximum value ΔG_*, which occurs at the critical radius r_c. A droplet has a tendency to grow when $r > r_c$ and reduces the free energy of the system by capturing molecules. Thus,

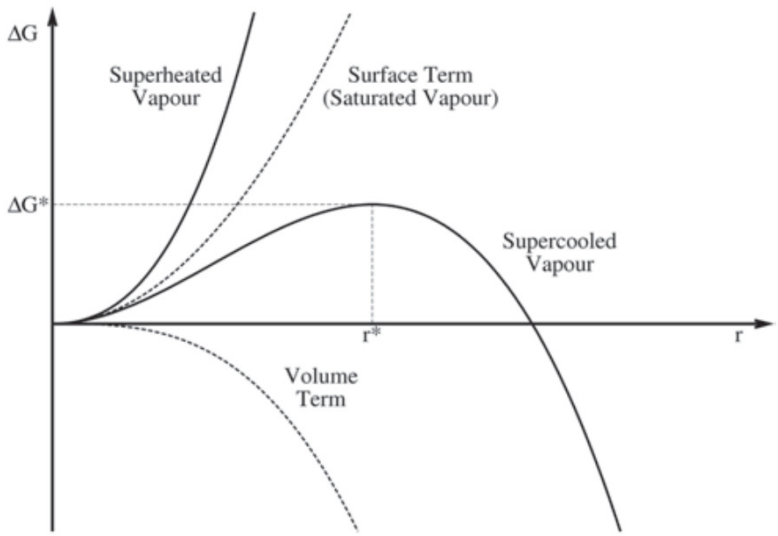

Figure 2.5: Variation of ΔG with r for supersaturated and superheated vapors, adapted from [2]

a critical droplet is in unstable equilibrium with the surrounding medium. Assuming that the vapor behaves as a perfect gas and ρ_l and σ depends only on the temperature T_g, it is possible to obtain expressions for ΔG_* and r_c differentiating Equation 2.20 with respect to r and equating to zero. The result is shown in Equations 2.22 and 2.23 :

$$\Delta G_* = \frac{4r_c^2\sigma}{3} = \frac{16\pi\sigma^3}{3(\rho_l R T_g \ln(S))} , \tag{2.22}$$

$$r_c = \frac{2\sigma}{\rho_l R T_g \ln(S)} , \tag{2.23}$$

Another formulation approaches with the concept of supercooling ΔT instead of supersaturation, although it appears more often in the literature, by its physical significance. The definition of $\Delta T = T_s(p) - T_g$, where $T_s(p)$ is the saturated vapor temperature at pressure p. Using the Clausius-Clapeyron equation, an appropriate relation between S and ΔT is defined by Equation 2.24:

$$\ln(S) = \frac{h_{fg}}{R T_s(p)} \frac{\Delta T}{T_g} , \tag{2.24}$$

where h_{fg} is the specific enthalpy of evaporation and thus, ΔG_* is the barrier to the formation of a droplet.

Equation 2.22 shows that S and ΔG_* are inversely proportional, so when S increases ΔG_* decreases; it never disappears completely.

The particle cluster formation process is discussed in more detail in [2]. An important result of the derivation of the expression for the classical nucleation rate per unit mass of

vapor represented as J_{CL}:

$$J_{CL} = q_c S \left(\frac{\rho_{gs}}{\rho_l} \right) \sqrt{\frac{2\sigma}{M^3 \pi}} \exp \left(- \frac{4\pi r_c^2 \sigma}{3kT_g} \right) , \tag{2.25}$$

where q_c is the condensation coefficient, ρ_{gs} is the specific mass of the supersaturated gas and $k = MR$ is Boltzmann's constant. The CL subscript stands for "Classical", as it is the classical nucleation rate formulation.

2.4.3 Corrections to the Classical Theory

With the advances in homogeneous nucleation studies, new corrections and refinements of the classical theory began to appear. Some of these will be discussed in this section, as some of them might contribute to a more robust modeling of the phenomenon.

There is an important parameter to be defined before presenting the corrections. In the literature, it is common to refer to a droplet of radius r comprising g molecules as a g-mer. If M is the mass of a molecule, the droplet mass is $4\pi r^3 \rho_l / 3 = gm$, and its surface area is calculated by $4\pi r^2 = A g^{2/3}$, where $A = 36\pi (M/\rho_l)^2$. Substituting into Equation 2.20, we have an equation in terms of g instead of r:

$$\frac{\Delta G}{kT_g} = \frac{A\sigma}{kT_g} g^{2/3} - g \ln(S) . \tag{2.26}$$

Now it is possible to proceed with Courtney's correction [20]. They verified that the effect of the partial pressure for systems with $g > 1$ was not taken into account in the classical theory. So, Equation (2.26) should read:

$$\frac{\Delta G}{kT_g} = \frac{A\sigma}{kT_g} g^{2/3} - (g-1) \ln(S) , \tag{2.27}$$

which do not alter the expressions for ΔG^* and r_c but the nucleation rate becomes:

$$J_{CTY} = q_c \left(\frac{\rho_{gs}}{\rho_l} \right) \sqrt{\frac{2\sigma}{M^3 \pi}} \exp \left(- \frac{4\pi\sigma}{3kT_g} r_c^2 \right) , \tag{2.28}$$

where the subscript CTY stands for Courtney correction.

Another refinement available in the literature is called non-isothermal nucleation. The deduction process made in the classical theory assumes that the vapor and droplet temperatures are equal. However, in some flows the temperature difference is crucial to driving the heat transfer between the vapor and liquid phases; this also leads to a different behavior in the nucleation rate, as it depends on the gas temperature. Kantrowitz [21] was one of the first to consider the problem, deriving a simple correction to the isothermal theory;

his work was later collaborated by Feder[22]. Kantrowitz's solution consists in multiplying the nucleation rate by a non-isothermal factor ϕ, defined below 2.29:

$$J_{NISO} = \phi J_{ISO} = \frac{J_{ISO}}{1+\xi} \,, \tag{2.29}$$

where J_{ISO} is the isothermal nucleation rate and can incorporate any appropriate correction. The ξ term is expressed in Equation 2.30:

$$\xi = \frac{\rho_g R}{\alpha_r} \sqrt{\frac{RT_g}{2\pi}} \frac{h_{fg}}{RT_g} \left(\frac{h_{fg}}{RT_g} - \frac{1}{2} \right) , \tag{2.30}$$

where α_r is the surface heat transfer coefficient of a critical droplet of radius r_c. At low pressures, the critical radius r_c is much smaller than the mean free path of a vapor molecule and the ideal-gas hypothesis is plausible. That way, Equation 2.30 can be simplified, with the factor γ being the ratio of specific heats of the vapor:

$$\xi = 2\frac{(\gamma-1)}{(\gamma+1)} \frac{h_{fg}}{RT_g} \left(\frac{h_{fg}}{RT_g} - \frac{1}{2} \right) . \tag{2.31}$$

As Bakhtar [2] concludes, there is not yet general agreement on the precise model for the nucleation rate, even for a largely researched substance such as water vapor. Most of the researchers tune the model with an adjustable factor to fit the experimental data. In this study, a series of numerical simulations will be evaluated with the classical nucleation rate and its corrections, as many authors do this kind of testing with different scenarios. Then, after validating the implementations in the OpenFOAM environment, a real supersonic-separator geometry will be analyzed with operational conditions.

Chapter 3

Mathematical Modeling

After extensive research and review of the literature, several ways of modeling the compressible, transient, and phase-change flow were discussed. Some of them carry a complex approach to the physics involved such as the multi-fluid model; others such as the mixture model and the source-term model consider a set of hypotheses, reducing the complexity of the system. Although the multi-fluid model is a more "complete" approach compared to others, many authors showed good agreement with experimental data capturing the homogeneous condensation phenomenon in supersonic nozzles, which is excellent to validate simulations because there are a lot of data available in the literature. With so, the proposal of the mathematical modeling here discussed is, in the simplest and physically accurate way possible, to describe and capture the homogeneous condensation phenomenon in supersonic flows.

3.1 Modeling of Homogeneous Condensation

The homogeneous condensation mathematical modeling selected for this work follows the classical nucleation theory, as defined in Equation 3.1. Corrections pointed out by Kantrowitz [21] and Courtney [20] will be validated as described in the Methodology section. Many authors did this validation test cases and reached results with good agreement with experimental data [16], [5].

$$J = q_c \frac{\rho_{gs}^2}{\rho_l} \sqrt{\frac{2\sigma}{\pi M_v^3}} \exp\left(-\frac{4\pi\sigma}{3kT_g} r_c^2\right) , \tag{3.1}$$

where q_c is a model constant. The droplet critical radius, r_c, which corresponds to the radius of the particles generated by the nucleation, is defined by the Equation 3.2:

$$r_c = \frac{2\sigma}{\rho_l R T \ln(S)} \ , \tag{3.2}$$

where σ is the superficial tension (different models will be discussed) and S is the supersaturation, which is defined by Equation 3.3:

$$S = \frac{p_v}{p_{sat}(T)} \ , \tag{3.3}$$

being p_v the condensable component partial pressure. *Dalton*'s law defines a relation between the partial pressure, mass fraction, and partial pressure of the component as described below by Equation 3.4:

$$p_v = y_c p \ , \quad \text{with} \quad y_c = \frac{(w_c/PM_c)}{\sum_{i=1}^{n} (w_i/PM_i)} \ , \tag{3.4}$$

where w_c is the mass fraction of the condensable component "c" in the mixture.

The particle growth rate was modeled following Young's model, represented by Equation 3.5 below [23]:

$$\frac{dr_d}{dt} = \frac{k\left[T_{sat}(p_v) - T\right]}{\rho_l h_{lg}\ r_d} \frac{(1 - r_c/r_d)}{\left[\dfrac{1}{1 + 2\beta K_n} + 3.78(1-\Theta)\dfrac{K_n}{Pr}\right]} \ , \tag{3.5}$$

where K_n is the *Knudsen* number defined in [4], [16] and [5], Pr is the *Prandtl* number, κ is the gas thermal conductivity and β is an adjustable parameter from the model. Θ is the modeling correction coefficient defined by Equation 3.6, where α is another model adjustable parameter.

$$\Theta = \frac{RT_{sat}}{h_{lg}} \left[\alpha - 0.5 - \frac{(2 - q_c)}{2q_c}\left(\frac{\gamma + 1}{2\gamma}\right)\left(\frac{C_p T_{sat}}{h_{lg}}\right)\right] \ . \tag{3.6}$$

3.2 Transport Equations

This section discusses the transport equations applied to the system. Some simplifying hypotheses were taken into account:

- Spherical droplets;
- Homogeneous Condensation;
- Latent heat of condensation is completely absorbed by gas phase;
- Phase-slip is neglected.

Therefore, one can formulate the transport equations of the system, where the conservation of mass, momentum, conservation of energy (written as a function of enthalpy), and the mass fraction of component "i" of the mixture are described by Equations 3.7, 3.8, 3.9 and 3.11 respectively:

$$\frac{\partial \rho}{\partial t} + \nabla \cdot (\rho \boldsymbol{U}) = -\dot{m}_{vl} \ , \tag{3.7}$$

$$\frac{\partial (\rho \boldsymbol{U})}{\partial t} + \nabla \cdot \Big(\rho \boldsymbol{U} \otimes \boldsymbol{U}\Big) = -\nabla p + \nabla \cdot \boldsymbol{\tau} - \dot{m}_{vl} \boldsymbol{U} \ , \tag{3.8}$$

$$\frac{\partial [\rho (h+K)]}{\partial t} + \nabla \cdot \Big[\rho \boldsymbol{U} (h+K)\Big] = \nabla \cdot \Big[\Big(\frac{\nu}{Pr} + \frac{\nu_t}{Pr_t}\Big) \nabla h\Big] + \frac{Dp}{Dt} + (\tau : \nabla \boldsymbol{U}) + \dot{m}_{vl}(h_{lg} - h) \ , \tag{3.9}$$

$$K = \frac{\boldsymbol{U} \cdot \boldsymbol{U}}{2} \ , \tag{3.10}$$

$$\frac{\partial \rho w_i}{\partial t} + \nabla \cdot (\rho w_i \boldsymbol{U}) = \nabla \cdot \left[\left(\frac{\nu}{Sc} + \frac{\nu_t}{Sc_t}\right) \nabla w_i\right] - \dot{m}_{vl} \ . \tag{3.11}$$

Where ν_t is the turbulent viscosity [24]. The closure problem will be solved with the turbulence model described in the next subsection. The Stress Tensor τ is calculated by means of Equation 3.12 below.

$$\tau_{ij} = -\left(\mu + \mu_t\right) \left[\left(\frac{\partial U_j}{\partial x_i} + \frac{\partial U_i}{\partial x_j}\right) - \frac{2}{3} \frac{\partial U_k}{\partial x_k} \delta_{ij}\right] + \underbrace{\frac{2}{3} \rho \kappa \delta_{ij}}_{\text{neglected}} \ . \tag{3.12}$$

The trace of the tensor which is marked as neglected is natively not implemented in the OpenFOAM framework, although it is important to consider it. That should be done in future works. Finally, the condensation rate $\dot{m}_{vl}$ is computed as:

$$\dot{m}_{vl} = \frac{4\pi r_c^3}{3} \rho_l J + 4\pi r_d^2 \rho_l N \frac{dr_d}{dt} \ , \tag{3.13}$$

where N (Number of particles by unit volume) is calculated by Equation 3.14:

$$\frac{\partial N}{\partial t} + \nabla \cdot (\boldsymbol{U} N) = J \ . \tag{3.14}$$

The droplets radii r_d is calculated by means of the generated liquid mass fraction W, according to Equation 3.15:

$$\overline{r_d} = \left(\frac{3\rho_g}{4\pi\rho_l} \frac{W}{(1-W)N}\right)^{1/3} \ , \tag{3.15}$$

and the transport equation for the generated liquid mass fraction is:

$$\frac{\partial(\rho W)}{\partial t} + \nabla \cdot (\rho \boldsymbol{U} W) = \dot{m}_{vl} \ . \tag{3.16}$$

3.2.1 Turbulence Models

The literature shows results from Nozzle simulations with good agreement with experimental data that disregards the effects of turbulence (inviscid flow). Since the main objective of this study is to apply the mathematical modeling to real operating conditions inside of a supersonic separator in which turbulence plays a major role, the better we describe the pressure and velocity fields the most accurate the results should be. Therefore, the Reynolds Average Navier-Stokes approach (RANS) was selected to solve the closure problem generated by the averaging process. For a complete deduction of the averaging process for the Navier-Stokes equations, refer to ARISTEU [25] or ATILA [26]. With that said, the $\kappa - \omega$ Shear-Stress Transport (SST) turbulence model was adopted for the validation cases.

The model was first proposed by Menter [27] aiming to get the best from the $\kappa - \epsilon$ and $\kappa - \omega$ models, and improving prediction in adverse pressure gradient boundary layers. In the wall region, the model behaves as the $\kappa - \omega$ model, while at the turbulent boundary layer, it assumes the $\kappa - \epsilon$ formulation. The model consists of two additional equations to the Navier-Stokes system: one for the turbulent kinetic energy κ and the other for the specific turbulent dissipation rate ω, given by Equations 3.17 and 3.18 below [28]:

$$\frac{D\rho\kappa}{Dt} = \nabla \cdot (\rho D_\kappa \nabla \kappa) + \rho G - \frac{2}{3}\rho\kappa\Big(\nabla \cdot \boldsymbol{U}\Big) - \rho\beta^*\omega\kappa + S_\kappa \tag{3.17}$$

$$\frac{D\rho\omega}{Dt} = \nabla \cdot \Big(\rho D_\omega \nabla \omega\Big) + \frac{\rho\gamma G}{\nu} - \frac{2}{3}\rho\gamma\omega\Big(\nabla \cdot \boldsymbol{U}\Big) - \rho\beta\omega^2 - \rho\Big(F_1 - 1\Big)CD_{\kappa\omega} + S_\omega \tag{3.18}$$

The turbulent viscosity, used in Equation 3.12, depends on κ and ω and is modeled according to Equation 3.19 below.

$$\nu_t = a_1 \frac{\kappa}{\max(a_1\omega, b_1 F_{23} \boldsymbol{S})} \tag{3.19}$$

For the supersonic separator geometry case, due to the strong rotational field imposed on the flow, the curvature correction term proposed by [29] has also been considered. The curvature correction relies on a rotation function f_{rot} in the turbulent kinetic energy production term.

3.3 Thermophysical Models

The equation of state employed in the cases for simulation validation follows the perfect gas assumption, Equation 2.6. Since the temperature and pressure conditions are low, it was considered plausible to use this simplification. Since condensation has a strong dependency on thermodynamic aspects of the flow, choosing the most accurate models to represent these effects is extremely important to the final results. Hence, instead of considering parameters such as specific heat and surface tension as constant values through the domain, models to capture the variation of these physical properties were used with the purpose to gather physical fidelity to the simulations. Furthermore, expressions to calculate the saturation pressure and the variation of viscosity with temperature were also used. Equation 3.20 shows the saturation pressure expression, which follows Antoines's Law:

$$\log_{10}(P_{sat}) = A - \frac{B}{T + C} \, , \tag{3.20}$$

The coefficients A, B, and C were taken from the NIST base, based on the model from Stull [30] [31]. The viscosity was calculated by the Sutherland model, presented by Equation 3.21 [32]:

$$\mu = A_s \frac{\sqrt{T}}{1 + T_s/T} \, . \tag{3.21}$$

The specific heat capacity was obtained by a polynomial adjustment with coefficients from tables NIST-JANAF, as in Equation 3.22 [33]:

$$C_p(T) = A + BT + CT^2 + DT^3 \tag{3.22}$$

The condensation enthalpy h_{lg} is evaluated by Watson's formula 3.23, as suggested in [4]:

$$h_{lg} = h_{lg0} \left[\frac{1 - T_r}{1 - T_{br}} \right]^n \tag{3.23}$$

where T_r is the reduced temperature and T_{br} is the reduced temperature at normal boiling point.

Chapter 4

Methodology

The methodology used to validate the mathematical modeling and the implementations will be presented in this chapter. Validation with experimental data from the literature is the first step, as two different cases of supersonic nozzles were chosen to compare the numerical and experimental results. The computational domain, mesh, and boundary conditions will be discussed, such as the numerical methods and solution algorithm applied.

4.1 Studied cases

The studied cases consist of two experiments of steam flow through supersonic nozzles used as validation for the implementation of mathematical modeling. The nozzle geometries correspond to Barschdoff [3] and Moore [34] experiments, respectively. The work of Jabir [16] brings a good comparison analysis of these geometries and three more, but for validation purposes, the two experiments cited above will meet the needs expected. Then, after comparison with experimental data and discussion of the results of different models of condensation rate, as explained in Chapter 3, an actual supersonic separator geometry developed by the research team at labCFD (School of Chemistry UFRJ) will be simulated to investigate its condensation efficiency and G force-generating capability. The latter is an important project aspect because in order to separate the condensed droplets the rotational field must be powerful [35].

4.1.1 Validation with Experimental Data

The experimental procedure from the works of Barschdoff [3] and Moore [34] are similar: a nozzle geometry inside a chamber is exposed to steam flow; pressure and temperature

are measured along the center line of the nozzle. A window is normally positioned by the nozzle in order to visualize shock waves and condensation through image techniques, as shown in Figure 4.1:

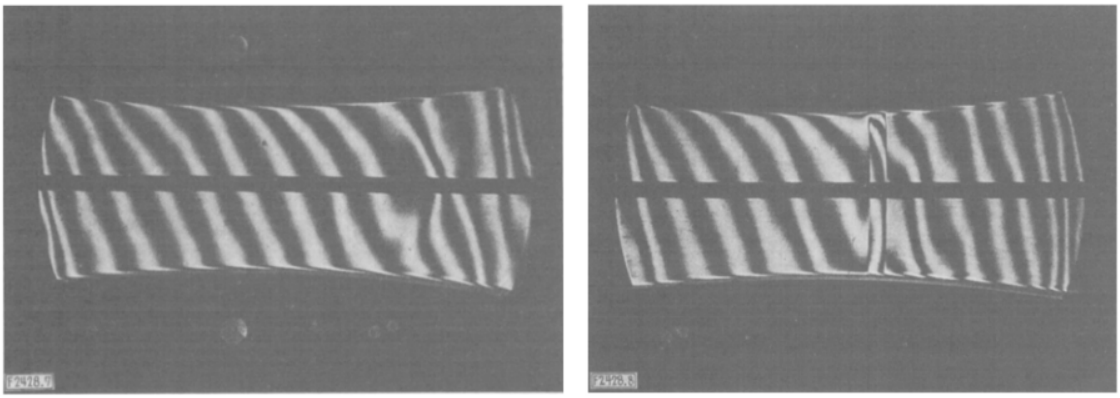

Figure 4.1: Condensation and shock wave formation inside the nozzle. Images from Barschdoff's work [3]

The objective is to gather information about the pressure, velocity, and temperature fields to infer when and where the condensation happens and under what conditions. Experiments with steam and nozzle geometries are broadly found in the literature, so plenty of experimental data is available for comparison.

4.1.2 Supersonic Separator

The supersonic separator geometry used in this work was developed and provided by the research team at labCFD UFRJ [35]. Since there is still not much experimental data available in the literature for this type of geometry, the validation will be done exclusively with the nozzle geometries.

To ensure a reasonable centrifugal force field, and consequently a good separation efficiency, the geometry proposed counts with 8 static helical blades positioned by the inlet, as shown in Figure 4.2:

Table 4.1 lists characteristics such as blade angle, number of blades, and thickness.

Table 4.1: Characteristics of the supersonic separator geometry.

Geometry	**Angle [degrees]**	**Nº of blades**	**Thickness [m]**
Supersonic Sep.	75	8	0.001

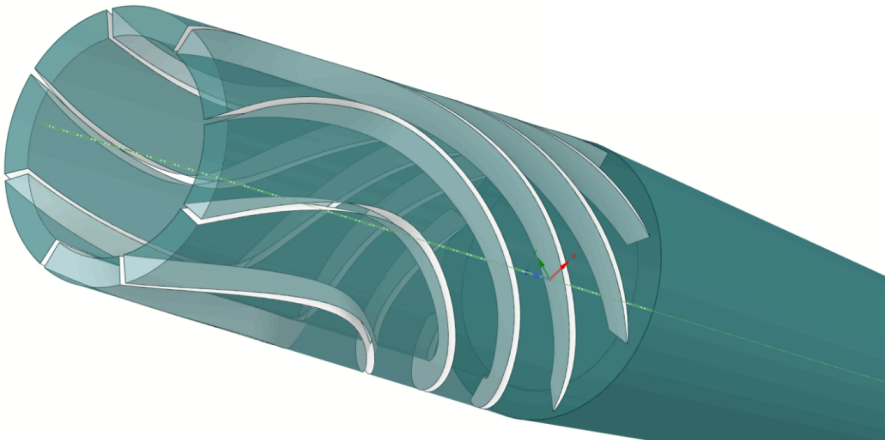

Figure 4.2: Detail of helical blades at the inlet of the supersonic separator.

The importance of the blades relies on the centrifugal force field that must be created in order to separate the condensed substance from the gaseous one. Since millions of 1 μm radius droplets are formed in the process, the highest G force possible must be generated. The convergent-divergent geometry helps to accelerate the flow and provides the necessary temperature and pressure conditions for the onset of condensation. The actual measures of the supersonic separator will not be presented due to confidentiality reasons.

4.2 Numerical Methods and Solution Algorithm

This work was developed in the OpenFOAM framework. OpenFOAM is a free, open-source software with large use in multiple engineering applications, such as complex fluid flows involving chemical reactions, turbulence, and heat transfer to acoustics, solid mechanics, and electromagnetism [28]. The condensation modeling was implemented using a native solver called `reactingFoam` as a starting point; its structure was highly reused. The software and its solvers are based on the classic Finite Volume Method (FVM) with a co-located arrangement.

For a complete explanation of the Finite Volume Method, refer to [36], [37], and [38]. The flowchart represented by Figure 4.3 corresponds to the pimple loop solving velocity, component mass fraction, energy, and pressure equations, also correcting fields to ensure mass conservation as condensation happens.

With that said, the new solver `homogeneousCondensationFoam` has its solution algorithm based on the `PIMPLE` algorithm: merged `SIMPLE-PISO` [39], [37]; while the linear

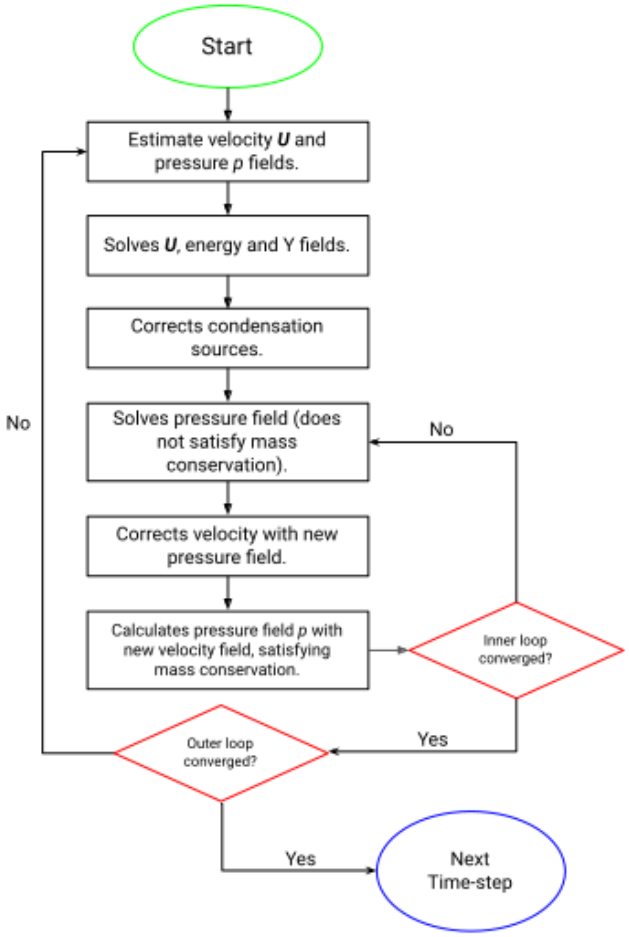

Figure 4.3: Flowchart of the solution algorithm

solvers are based on the conjugated gradients and algebraic multi-grid method (GAMG). The methods chosen for the simulations carried out in this study were all of second order of accuracy for the advective term (linear Upwind) and the TVD Minmod [28]; for the gradient operator, the pointCellsLeastSquares was chosen and the interpolation method is linear.

4.2.1 LTS Method

The LTS method (*Local Time Scale*) integrates the equations using a local time scale to reach the steady-state, following equations 4.1 and 4.2 below:

$$(\Delta t_P)_{LTS} = 2Co_{max} \left[\frac{\sum_f (\rho \parallel \boldsymbol{U} \cdot \boldsymbol{S} \parallel)_f}{\rho V} \right]_P^{-1} \tag{4.1}$$

$$\Delta t_P = \min \left[(\Delta t_P)_{LTS}, \Delta t_{max} \right] \tag{4.2}$$

where Co_{max} and Δt_{max} are the Courant number and the user-supplied maximum time step. The advantage of using a local time scale in these simulations is that the steady state is reached more rapidly in regions where a detailed time solution is not required, such as regions where the flow is subsonic or there is no condensation. On the other hand, regions that demand good time resolution and the physical phenomenon involved happens very fast, are solved with a smaller local time step.

4.3 Domain and Boundary Conditions

This section will focus on the computational domain (geometry and mesh) of the studied cases as well as the boundary conditions employed. Section 4.3.1 refers to the validation cases and 4.3.2 refers to the supersonic separator case.

4.3.1 Validation cases

Figures 4.4 and 4.6 show the geometries of both nozzles simulated for the validation with experimental data. The first one, Barschdoff's nozzle [3] is a circular arc nozzle with

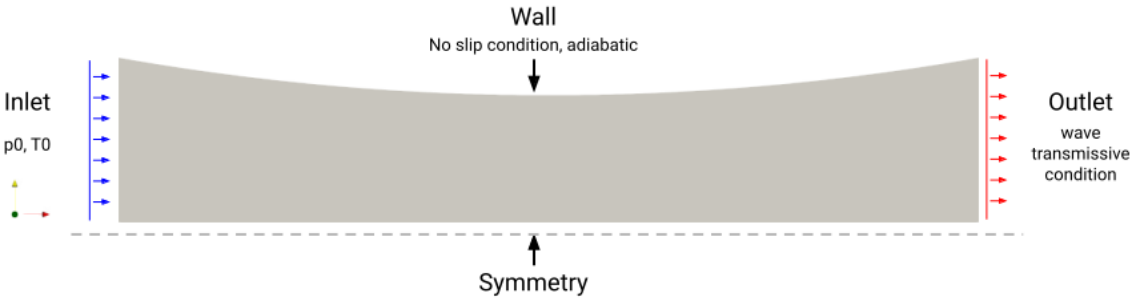

Figure 4.4: Barschdoff's nozzle geometry

584 mm wall curvature and 200 mm length. The total pressure at the inlet is set to $78,39$ kPa at a total temperature of $380,6$ K as defined in table 4.2 along with other boundary conditions. Since the geometry is axisymmetric, only half of the domain was simulated using a symmetry condition as pointed out in the figure above, to reduce computational cost.

The conditions `kLowRe`, `nutUSpalding`, and `omegaWallFunction` implement low reynolds laws of the wall in OpenFOAM [40], [41]. Conditions `totalPressure` and `totalTemperature` implement conditions of type 1 (Dirichlet) for pressure and temperature based on isentropic relations of gases:

$$p_b = p_0 \left[1 + \frac{\gamma - 1}{2} M_a^2\right]^{\frac{\gamma - 1}{\gamma}} \quad , \quad T_b = T_0 \left[1 + \left(\frac{\gamma - 1}{2} M_a^2\right)\right]^{-1}$$

where b is the index of the contour faces, p_0 and T_0 are stagnation pressure and temperature inputed by the user, γ is the specific heat ratio and M_a is the Mach number given by equation 4.3:

$$Ma = \frac{\parallel \boldsymbol{U} \parallel}{\sqrt{\gamma R T}} \tag{4.3}$$

Condition `pressureInletVelocity` evaluates velocity at the boundaries where pressure is specified. The velocity is obtained from the calculated flux in the contour faces following equation 4.4 below:

$$\vec{U}_{n,b} = \left[\frac{\boldsymbol{n}\phi}{\rho \parallel \boldsymbol{S} \parallel}\right]_b \quad \text{where} \quad \phi_b = (\rho \boldsymbol{U} \cdot \boldsymbol{S})_b \tag{4.4}$$

where $\boldsymbol{n}$ is the surface normal unity vector. Condition `pressureInletOutletVelocity` is similar, but depends on the signal of the flux on the contour face:

$$\phi_b > 0 : \qquad \boldsymbol{n} \cdot \nabla \boldsymbol{U} = \boldsymbol{0} \tag{4.5}$$

$$\phi_b < 0 : \quad \boldsymbol{U}_{n,b} = \left[\frac{\boldsymbol{n}\phi}{\rho \| \boldsymbol{S} \|}\right]_b \tag{4.6}$$

Finally, condition `waveTransmissive` is a specialization of an advective outlet condition made to avoid reflections caused by shock waves at the contours [28]. The succeeding problem is solved at the boundary:

$$\left[\frac{D(wp)}{Dt}\right]_b = 0 \tag{4.7}$$

where w is the wave velocity at the contour defined by:

$$w_b = \left[\frac{\phi}{\rho \parallel \boldsymbol{S} \parallel} + \sqrt{\frac{\gamma R T}{M}}\right]_b \tag{4.8}$$

the parameters l_∞ and p_∞ are a length and value scale of the far-field supplied by the user and utilized as mechanisms of under-relaxation at the solution of the contour equation above [39].

Three computational meshes were tested to guarantee that the solution is independent of the mesh. Figure 4.5 shows the three meshes simulated, going from the coarsest (1) to the finest (3). All of the geometries and meshes for the validation cases were generated in Salome-Meca, an open-source python-based software [42]. Table 4.3 lists the number

Table 4.2: Boundary conditions of Barschdoff's nozzle validation case

Variable	**inlet**	**outlet**	**wall**
U	pressureInletVelocity	pressureInletOutletVelocity	$\boldsymbol{U} = (0, 0, 0)$
T	totalTemperature	$\boldsymbol{S} \cdot \nabla T = 0$	$\boldsymbol{S} \cdot \nabla T = 0$
	$T_0 = 380.6[K]$		
p	totalPressure	waveTransmissive	$\boldsymbol{S} \cdot \nabla p = 0$
	$p_0 = 78,39[kPa]$; $\gamma = 1.385$	$\gamma = 1.385$; $l_\infty = 5[m]$	
k	$\kappa = \frac{3(IU)^2}{2}$, $I = 5[\%]$	$\boldsymbol{S} \cdot \nabla \kappa = 0$	kLowReWallFunction
omega	$\omega = \frac{C_\mu \sqrt{\kappa}}{l}$, $l = 28[mm]$	$\boldsymbol{S} \cdot \nabla \omega = 0$	omegaWallFunction
nut	$\nu_t = \frac{C_\mu \kappa}{\omega}$	$\nu_t = \frac{C_\mu \kappa}{\omega}$	nutUSpaldingWallFunction
Steam—W—N	$w_{steam} = 1.0;\ W = 0;\ N = 0$	$\boldsymbol{S} \cdot \nabla (w_{steam} \vert W \vert N) = 0$	$\boldsymbol{S} \cdot \nabla (w_{steam} \vert W \vert N) = 0$

of elements and other parameters of the meshes such as aspect ratio (A.R) and maximum values of mesh skewness and non-orthogonality as defined by OpenFOAM. Since the geometry of this nozzle is the main region of analysis, the discretization procedure employed was focused on generally reducing the element size. As condensation is a very fast phenomenon, the element size plays an important role in the capture of this reduced time-scale effect.

Moore's nozzle [34] (Nozzle B in Moore's work) is larger than the previous one although it has the lowest inlet total pressure - $25kPa$ - and a total temperature of $358.1K$. Unlike Barschdoff's nozzle, this one has a sharp corner at the throat, which has already been reported that this kind of geometrical aspect can lead to the formation of expansion waves within the flow, which in turn changes the condensation zone and consequently the pressure distribution. An aspect of experiments with nozzles is the possibility to achieve supersonic flows without having the formation of expansion or shock waves due to the smooth transition of the geometry. Figure 4.6 shows the geometry of the nozzle and its boundaries; boundary conditions are fundamentally equal to the previous case, they differ only in the total pressure and temperature values.

The same methodology for mesh convergence was employed as three computational meshes were made. The area near the throat was the discretization target since the fastest phenomenon happens there (nucleation of particles).

Figure 4.7 shows the three meshes used for the convergence test and table 4.4 lists their

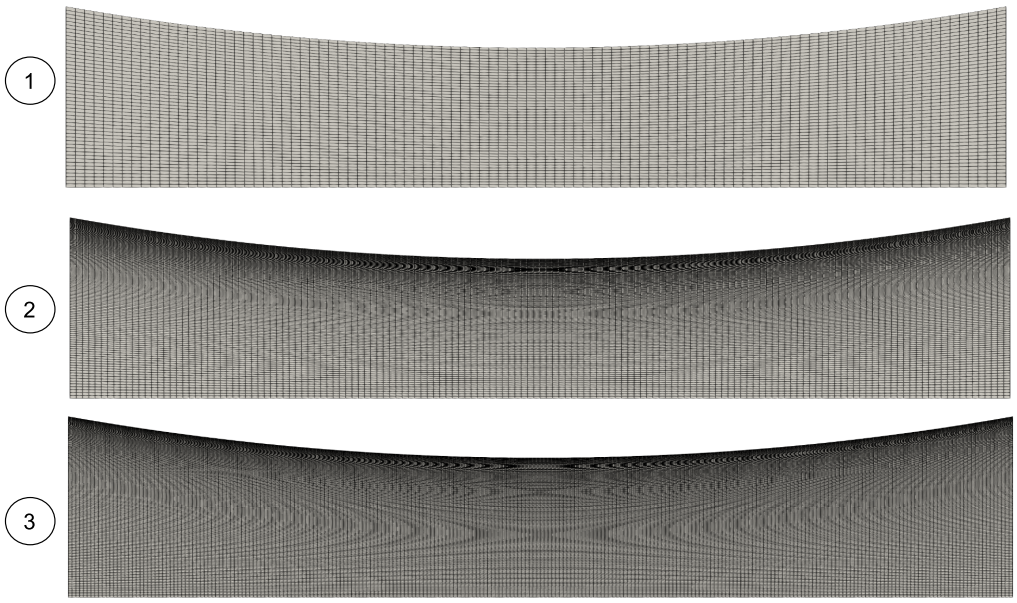

Figure 4.5: Computational meshes for Barschdoff's nozzle

Table 4.3: Mesh parameters for Barschdoff's nozzle validation case.

Mesh	**Elements**	**A.R.**	**Max Skewness**	**Non-Orthogonality**
1	5000	3,38	0,43	3,4
2	24900	33,85	0,43	4,5
3	48750	98	0,43	4,3

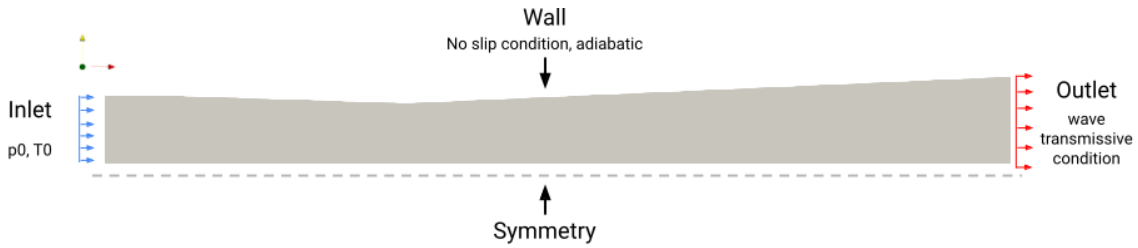

Figure 4.6: Moore's nozzle geometry

parameters. Two variables were analyzed to determine the mesh independency: pressure and temperature distributions. When the error between the results of certain points in the domain became less than 1%, the mesh was considered converged. After validating the implementation, the supersonic separator was simulated. The mesh was built with Pointwise, a software with advanced functions to build complex and high-fidelity meshes.

Table 4.4: Mesh parameters for Moore's nozzle validation case.

Mesh	Elements	A.R.	Max Skewness	Non-Orthogonality
1	3300	7,5	0,1	1.5
2	47300	11,06	0,1	1,6
3	136800	17,4	0,1	1,6

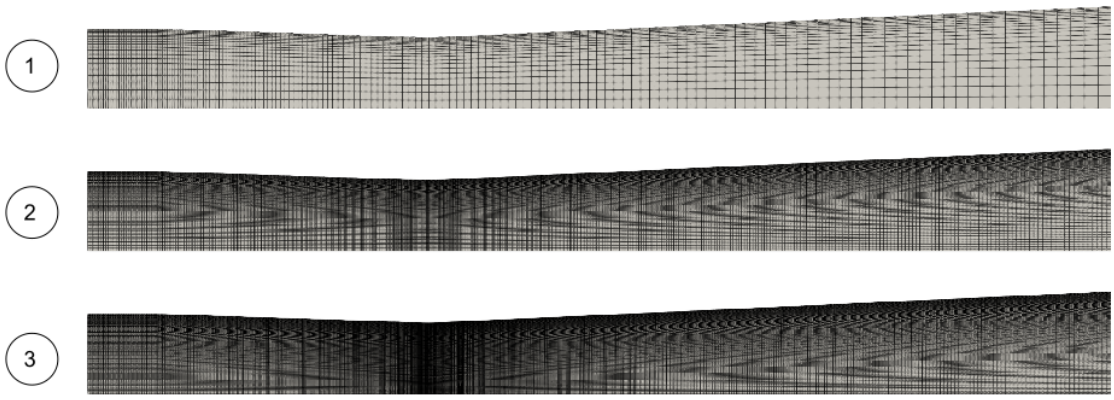

Figure 4.7: Computational meshes for Moore's nozzle

4.3.2 Supersonic separator

Figure 4.8 shows the computational domain of the supersonic separator. Despite the centrifugal force field and the rotational flow, it is possible to represent the full behavior of the flow inside the separator simulating only a fraction of it due to its axial symmetry, as shown in [43]; with a smaller domain, it is possible to create a fine mesh in the most important regions (near-throat areas) and maintain a relatively light mesh, reducing the computational cost.

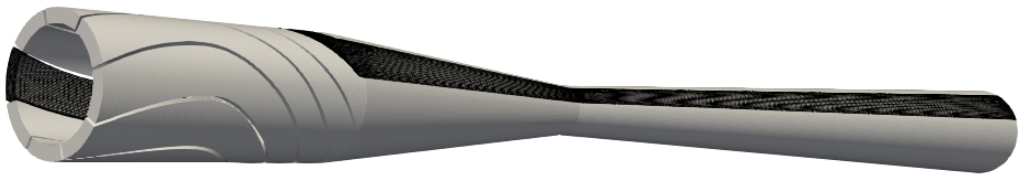

Figure 4.8: Supersonic Separator's mesh

The entire geometry is gray while the simulated region is marked with the control volumes; it represents 1/8 of the entire domain and periodic boundary conditions were used to represent the full flow. Table 4.5 shows the parameters of the mesh:

Table 4.5: Mesh parameters for supersonic separator geometry.

elements	max $-nonOrtho$	max $-skewness$	max $-AR$
361137	61	1.15	149.2

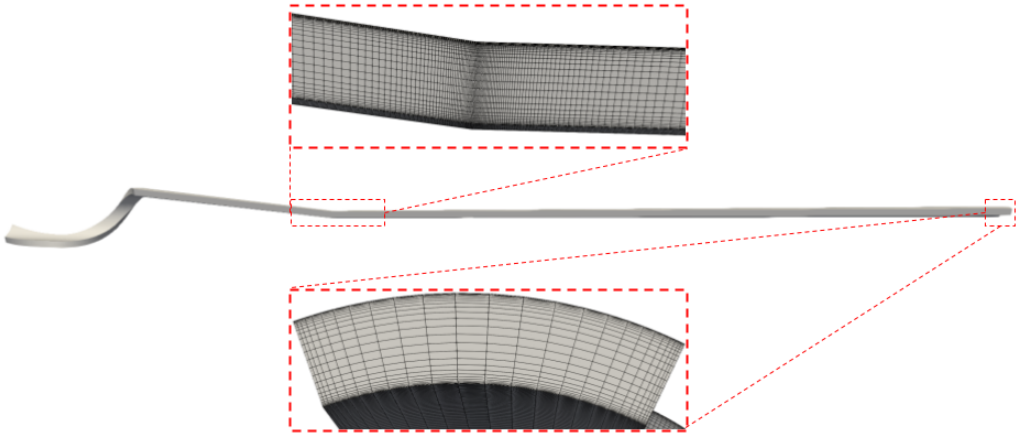

Figure 4.9: Supersonic separator's mesh with details at the throat and angular direction.

Besides that, figure 4.9 shows more details about the mesh, for example, its refinement regions. Special attention was given to the refinement near the walls, to fulfill the requirements of the turbulence model.

Table 4.6: Boundary conditions of the supersonic separator case

Variable	**inlet**	**outlet**	**wall**
U	pressureInletVelocity	pressureInletOutletVelocity	$\boldsymbol{U} = (0, 0, 0)$
T	totalTemperature	$\boldsymbol{S} \cdot \nabla T = 0$	$\boldsymbol{S} \cdot \nabla T = 0$
	$T_0 = 233[K]$		
p	totalPressure	waveTransmissive	$\boldsymbol{S} \cdot \nabla p = 0$
	$p_0 = 8[MPa]$; $\gamma = 1.385$	$\gamma = 1.385$; $l_\infty = 5[m]$	
k	$\kappa = \frac{3(IU)^2}{2}$, $I = 5[\%]$	$\boldsymbol{S} \cdot \nabla \kappa = 0$	kLowReWallFunction
omega	$\omega = \frac{C_\mu \sqrt{\kappa}}{l}$, $l = 28[mm]$	$\boldsymbol{S} \cdot \nabla \omega = 0$	omegaWallFunction
nut	$\nu_t = \frac{C_\mu \kappa}{\omega}$	$\nu_t = \frac{C_\mu \kappa}{\omega}$	nutUSpaldingWallFunction
CO2—W—N	$w_{co2} = 0.4$; $W = 0$; $N = 0$	$\boldsymbol{S} \cdot \nabla(w_{co2}\|W\|N) = 0$	$\boldsymbol{S} \cdot \nabla(w_{co2}\|W\|N) = 0$

Chapter 5

Results

This chapter aims to present and discuss the results of the simulations driven through this study. There are two main sections: modeling validation and the supersonic separator's results. For the validation results, pressure distribution along the center line of the nozzles was compared between CFD and experimental data; Moore's nozzle present also data for the droplet radius, which is not present in Barschdoff's work.

5.1 Modeling Validation

In this section, we will discuss the results of the simulations of both nozzles presented in this text. A mesh convergence test was made for each case to ensure mesh independence; distributions of temperature, pressure, and nucleation rate were considered the main variables to capture in this process. For the validation cases with Moore's nozzle [34], a comparison with Jabir's simulation data [16] will be made.

5.1.1 Moore's Nozzle

The first step made was the mesh convergence procedure. For the three meshes, the pressure, temperature, and nucleation rate distributions were plotted along the center line of the domain. Figure 5.1 below shows the ratio of pressure at the center line to the stagnation pressure and the temperature field; x^* is the distance from the throat. It can be seen that both medium and fine meshes give, basically, the same result; coarse mesh tends to diffuse a little bit more the pressure distribution, not being able to capture it completely.

It can be also seen that the coarse mesh does not capture with good accuracy the

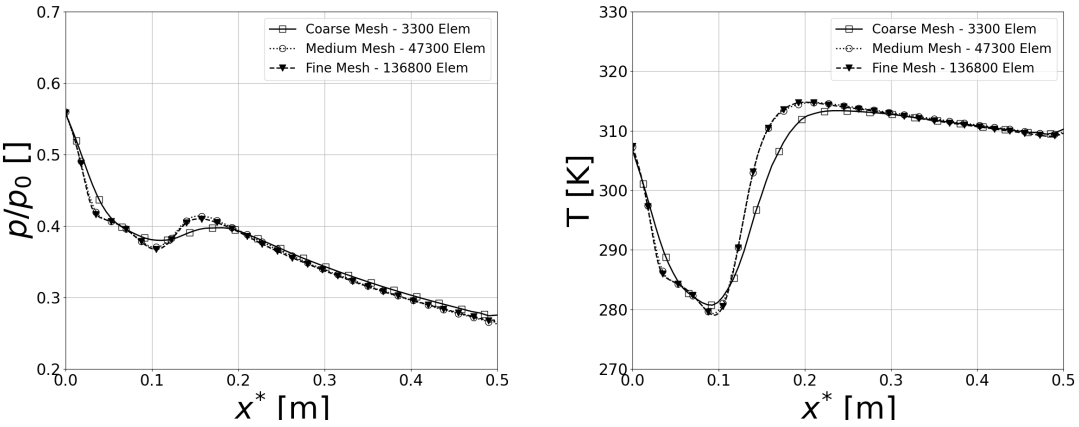

(a) Pressure by stagnation pressure ratio. (b) Temperature distribution comparison.

Figure 5.1: Mesh convergence analysis for Moore's nozzle.

temperature field in the same way that both medium and fine meshes do. Finally, the nucleation rate along the center line was also plotted. For better visualization, the logarithm of the nucleation rate is shown below, in figure 5.2: Following the previously observed

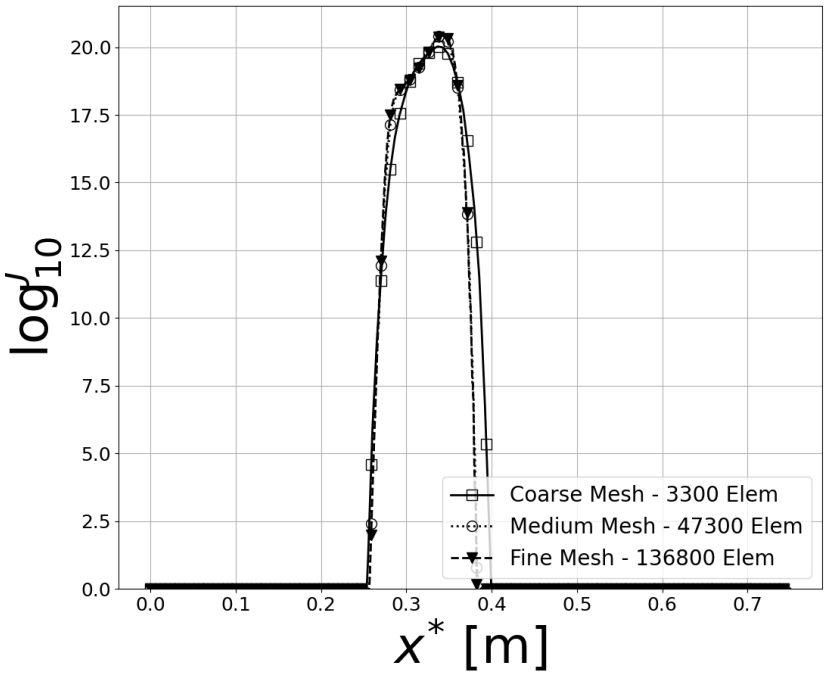

Figure 5.2: Nucleation rate distribution comparison.

behavior, the coarse mesh could not precisely capture the nucleation rate like the other meshes. Since both medium and fine meshes achieved basically the same results, with the relative error from successive meshes being less than 1%, capturing with a good agreement

the three variables proposed, the medium mesh was chosen for the cases as it requires less computational effort and time to simulate.

The next step is to present the results obtained with the simulation of Moore's nozzle. Three nucleation models were tested and compared:

- Classic nucleation theory model;
- Courtney's correction;
- Kantrowitz's non-isothermal correction.

The nucleation model impacts the dynamics of the flow, so fields such as pressure, temperature, nucleation rate, and mass source term should be impacted by the different models applied. However, this study will focus on the suitability of each model for the experimental data, in other words, which model represents and captures best the condensation inside the nozzle with respect to the experimental data. So, plots for pressure and temperature distribution, besides the nucleation rate, mass transfer, number of droplets generated, droplet radius and mass fraction of condensed steam will be presented only for this first case. For the qualitative analysis, figures from only one nucleation model will be presented, since there are not so many differences between them; it will be better exposed in the quantitative analysis. In that way, figure 5.3 below shows the steady-state velocity field for Moore's nozzle, which shows the high velocities reached. It can be seen that the flow accelerates as it passes through the throat of the geometry. It is important to remember that this is only half of the geometry, as the simulation was done with axisymmetric boundary conditions. A maximum Mach number of 1.4 was achieved inside the nozzle. Also, it can be seen that there is a huge pressure drop near the throat. This is generally the region where condensation happens because the pressure and temperature conditions become favorable. Figure 5.4 below shows the comparison of pressure distribution along the center line for the three models tested and the experimental data.

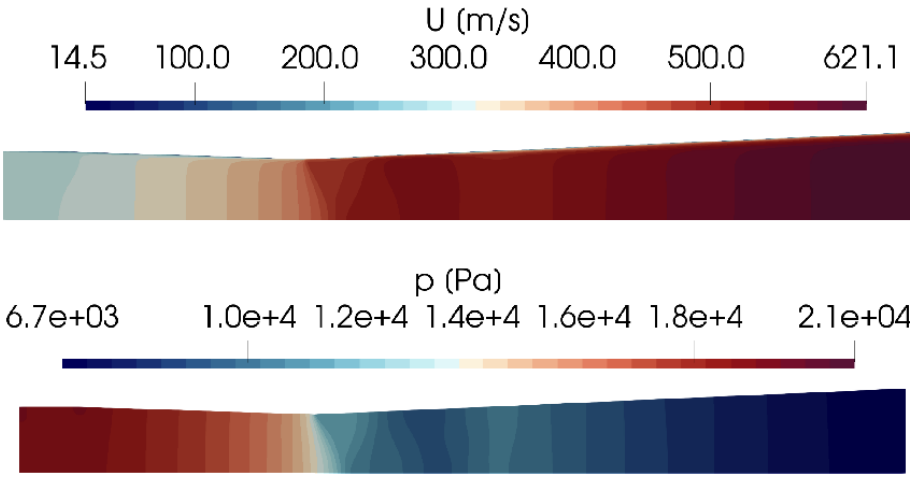

Figure 5.3: Velocity and pressure fields for Moore's nozzle.

It is noticeable that the Classic model and Courtney's correction capture the condensation onset (between 0.05 m and 0.09 m) before the starting point observed from the experimental data (0.1 m), while Kantrowitz's correction captures it with good agreement. On the other hand, the three models fail to capture with accuracy the pressure after the condensation point, overestimating it. Tests have been made with different boundary con-

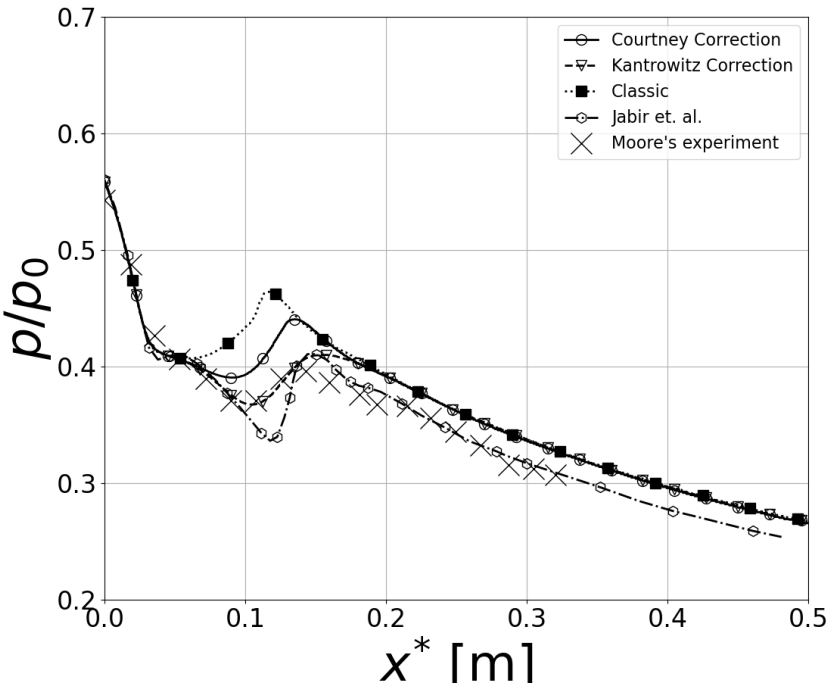

Figure 5.4: Pressure over stagnation pressure along center line comparison.

ditions, but the result remained the same, pointing to another cause for this behavior, which showed to be independent of the nucleation model. Jabir's simulation [16] captures

with a good agreement the final temperature, but does not capture the onset of the condensation. It is not defined in his work the thermophysical modeling used to simulate, nor the values of specific heat at constant pressure; in addition, the steam is not considered a perfect gas as he uses another equation of state. Figure 5.5 shows the temperature field inside the nozzle: it is possible to notice that the highest temperatures are reached at the

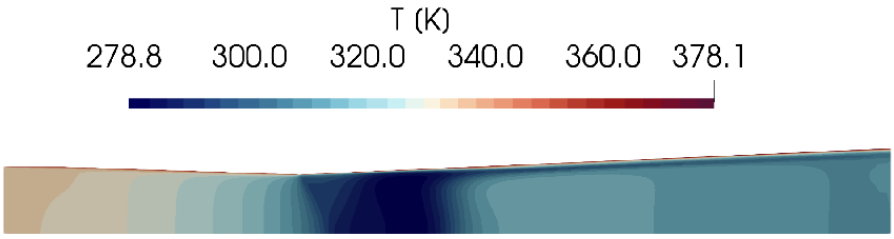

Figure 5.5: Temperature field inside Moore's nozzle.

walls of the nozzle, due to the viscous dissipation. At the throat area of the domain, the lowest temperatures are reached due to the pressure drop: 278.8 K or 5.65°C. Figure 5.6 shows a comparison between nucleation models for the temperature distribution along the center line of the nozzle. Unfortunately, there is no experimental data available: Once

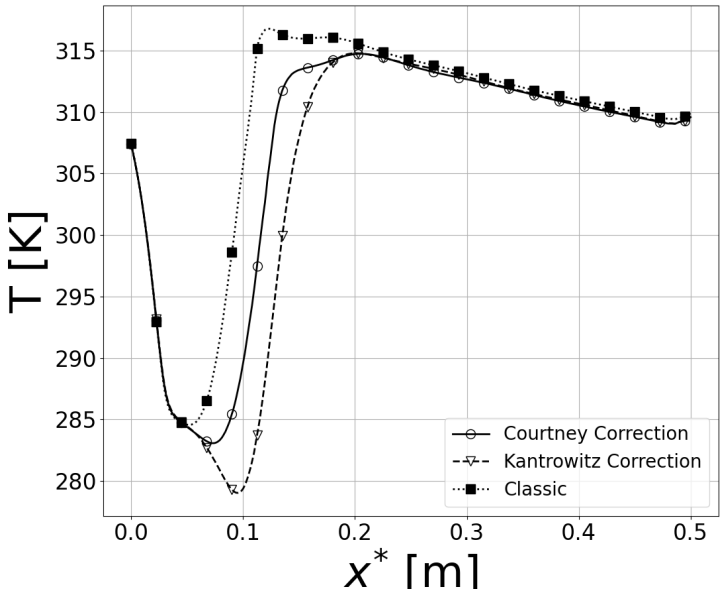

Figure 5.6: Temperature field along the center line for different nucleation models.

more, the three models capture the same final temperature, with similar behavior to the pressure distribution. Kantrowitz's correction reaches the lowest temperature of the models with 278.8 K, while Courtney's correction and the Classic model start the condensation

at higher temperatures. The increase in temperature is due to the heat released during the condensation of steam, behavior that is not seen in an isentropic scenario.

Other experimental data available in Moore's work is the droplet radius, which is compared in figure 5.7 below. Data from Jabir's work [16] is also introduced in this comparison.

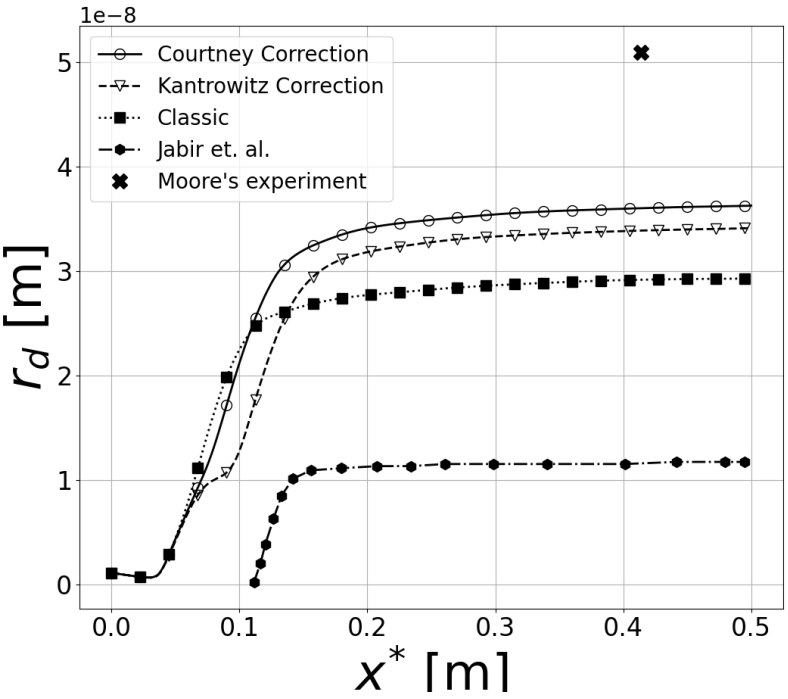

Figure 5.7: Droplet radius comparison.

Unfortunately, there is only one point available to compare with CFD simulations. Courtney's correction radius was a little bit bigger than Kantrowitz's, although both of them are very similar. The onset of the particle radius begins just before the throat, which can be related to the critical radius value formed before the actual condensation. Table 5.1 shows the percentual relative difference $R.D$ from the maximum value of radius reached against the experimental data.

Table 5.1: Relative difference percentual of maximum droplet radius in Moores' nozzle.

Data	Value $[10^{-8}m]$	R.D. [%]
Experiment	5.0909	-
Courtney's Corr.	3.6246	28.8
Kantrowitz's Corr.	3.41023	33
Classic	2.92766	42
Jabir et. al	1.17171	76.9

The following figures represent the variables related to the condensation fields, such as nucleation and mass transfer rate 5.8, supersaturation, liquid mass fraction, and the number of generated droplets 5.9. The nucleation only occurs in a specific spot in the

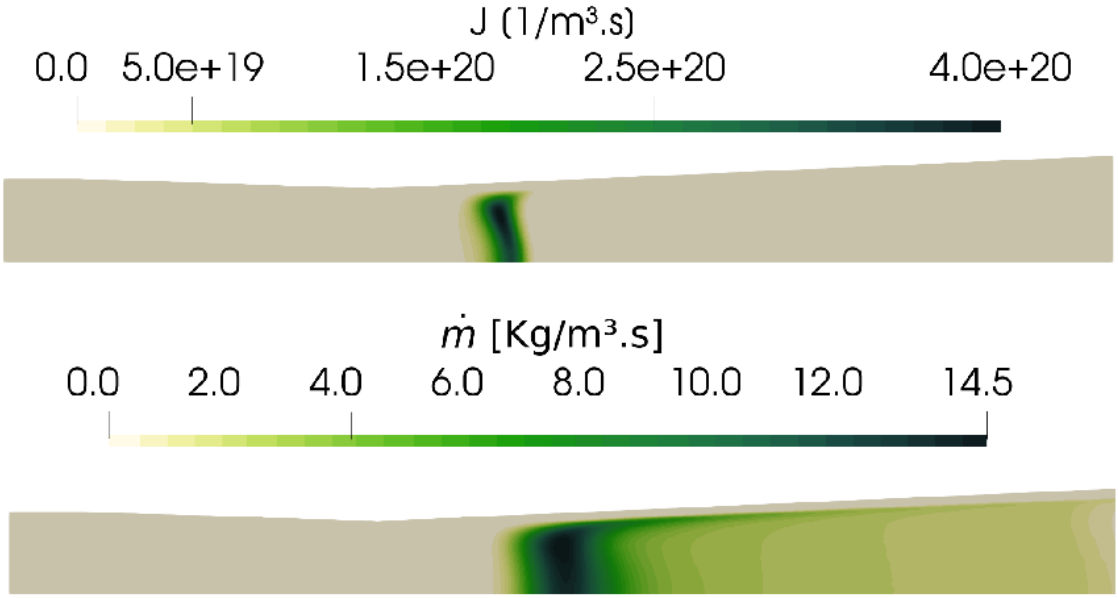

Figure 5.8: Nucleation rate and mass transfer rate fields: Kantrowitz correction model.

domain, as can be seen by the nucleation rate field. Because of the supersaturated state that the steam reaches, there is a type of delay in the condensation, which occurs right after the throat. The mass transfer is also bigger around the throat area, which is the main region of condensation. The image below shows the supersaturation degree reached in the

flow. A maximum supersaturation degree of 10.5 is reached near the throat region. All of these variables impact the nucleation and condensation of the steam. The liquid mass concentrates at the center of the nozzle, and only appears right after the throat, where is the onset of the condensation. A fraction of 4.3% of water is generated at the end of the supersonic nozzle. It is interesting to notice that the liquid concentration near the walls is nearly null due to the high temperatures reached in that region, which prevent the steam to condensate. The number of particles generated from the condensation has a magnitude of 10^{16}; with an Euler-Lagrange approach, this magnitude of droplets generated would have to be modeled as a "cloud" of particles, which would be very expensive computationally.

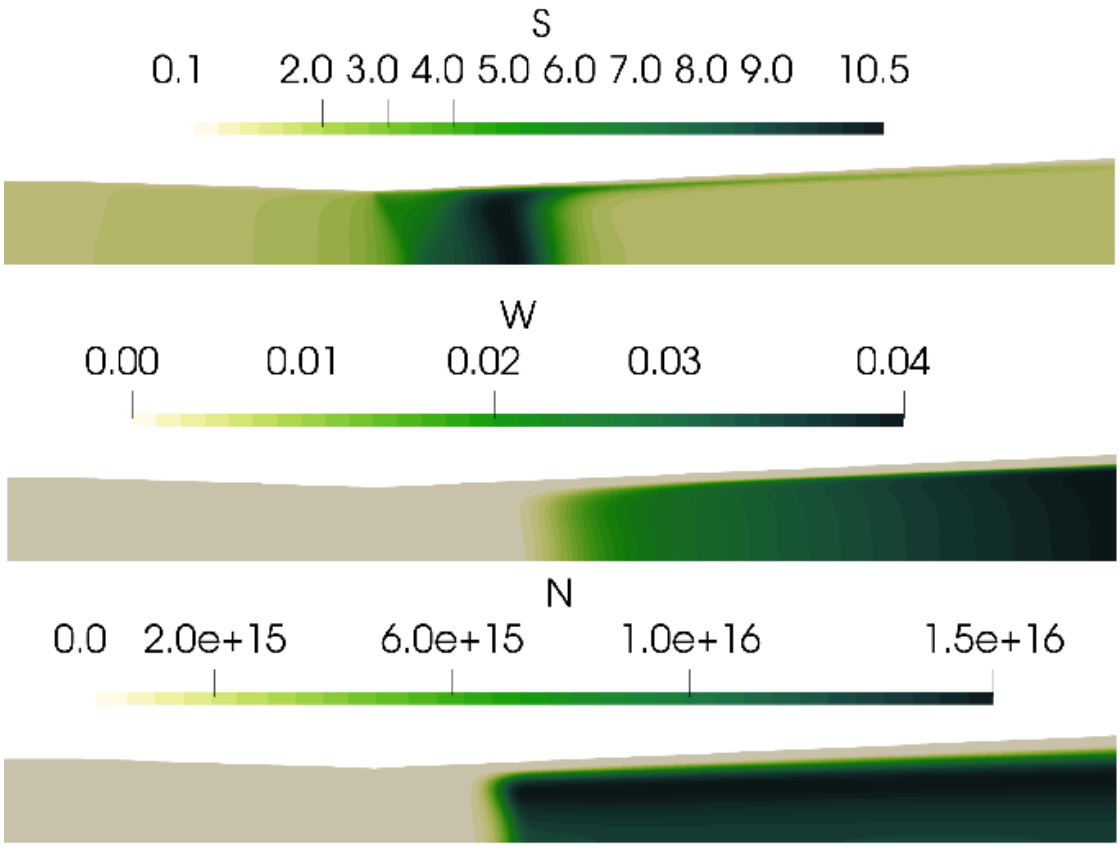

Figure 5.9: Supersaturation degree, liquid mass fraction, and number of generated particles fields.

5.1.2 Barschdoff's Nozzle

In this subsection, Barschdoff's nozzle validation simulation results will be presented and discussed. This scenario has a higher pressure and temperature than the previous one, as shown in Table 4.2: stagnation pressure at the inlet is equal to 78.39 [kPa] and temperature is equal to 380.6 [K]. As previously done, the mesh convergence results will

be shown first. Temperature, pressure, and nucleation rate were the variables chosen to determine the refinement of the mesh. Figure 5.10 below shows the static by stagnation pressure ratio and Temperature distributions alongside the center-line of the nozzle, which shows good results for all three meshes; the coarser one is a little diffusive at 0.075 m from the throat, similar to Moore's nozzle result.

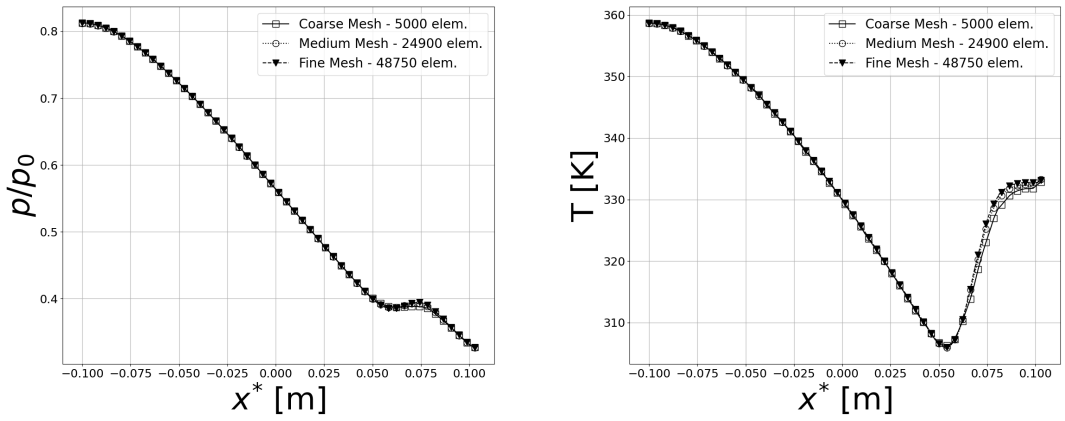

(a) Pressure by stagnation pressure ratio. (b) Temperature distribution comparison.

Figure 5.10: Mesh convergence analysis for Barschdoff's nozzle.

It can be seen in the figure above that the fine and medium meshes give practically the same results while the coarser one is slightly different at the end of the nozzle. Figure 5.11 shows the nucleation rate distribution:

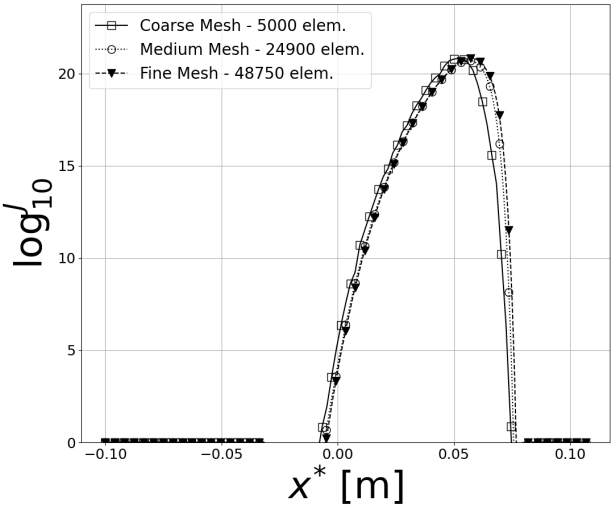

Figure 5.11: Logarithm of the nucleation rate distribution.

In this case, a more visible difference can be seen from the results of the coarse mesh

compared to others. Since both medium and fine meshes captured similar distributions of pressure, temperature, and nucleation rate and the relative error between meshes satisfied the criterium of being less than 1%, the medium one was chosen to reduce simulation time and computational effort. Proceeding to the qualitative analysis of the flow, figure 5.12 shows the velocity and pressure fields inside the supersonic nozzle, which achieves a maximum velocity value of 604 [m/s] approximately. Again, the fields shown below correspond to the Kantrowitz correction nucleation model. It is important to remember

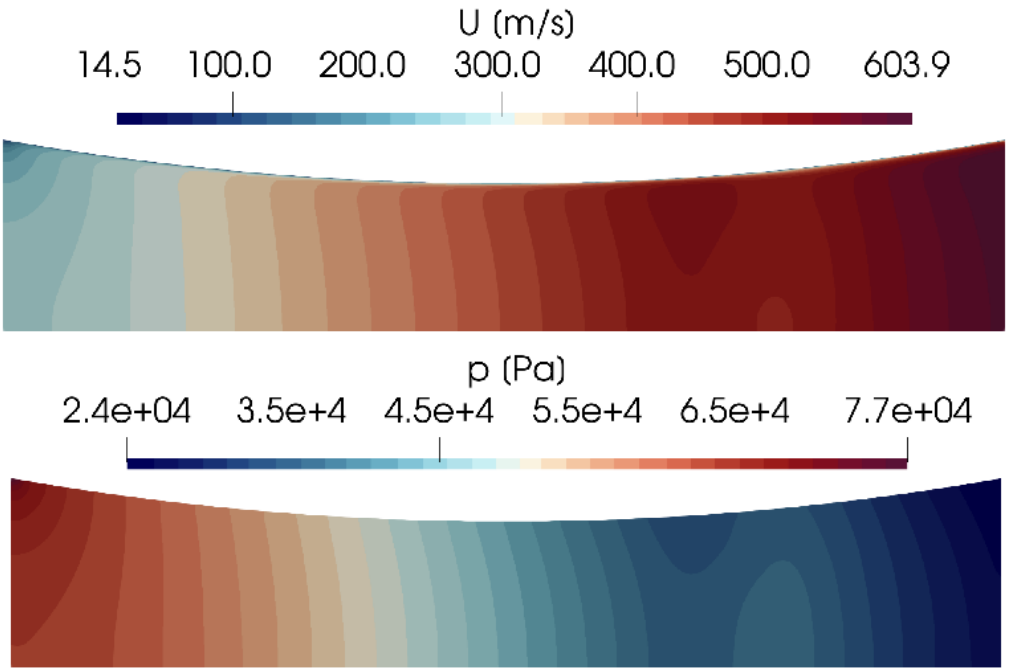

Figure 5.12: Velocity and pressure fields inside Barschdoff's nozzle.

that the geometry shown above is only half of the original domain and symmetry conditions were applied to reduce the mesh size. The steam accelerates as it passes through the narrower part of the geometry, reaching supersonic velocities. The figure above also shows the pressure distribution field, which does not show the formation of shock waves, due to the geometry of the nozzle. In fact, is better to have a geometry where the shock wave doesn't occur but the flow transit from subsonic to supersonic in a smooth way. Figure 5.13 below shows the comparison of the pressure distribution alongside the center line of the nozzle for the three nucleation models tested. In this case, none of the models tested captured with good precision the onset of the condensation; Kantrowitz's correction had the best result of them but is not too close to the point where the experimental data shows that the condensation starts. Throughout the tests for this study, all of the simulation's results showed to be very sensitive to the thermophysical properties, especially the specific

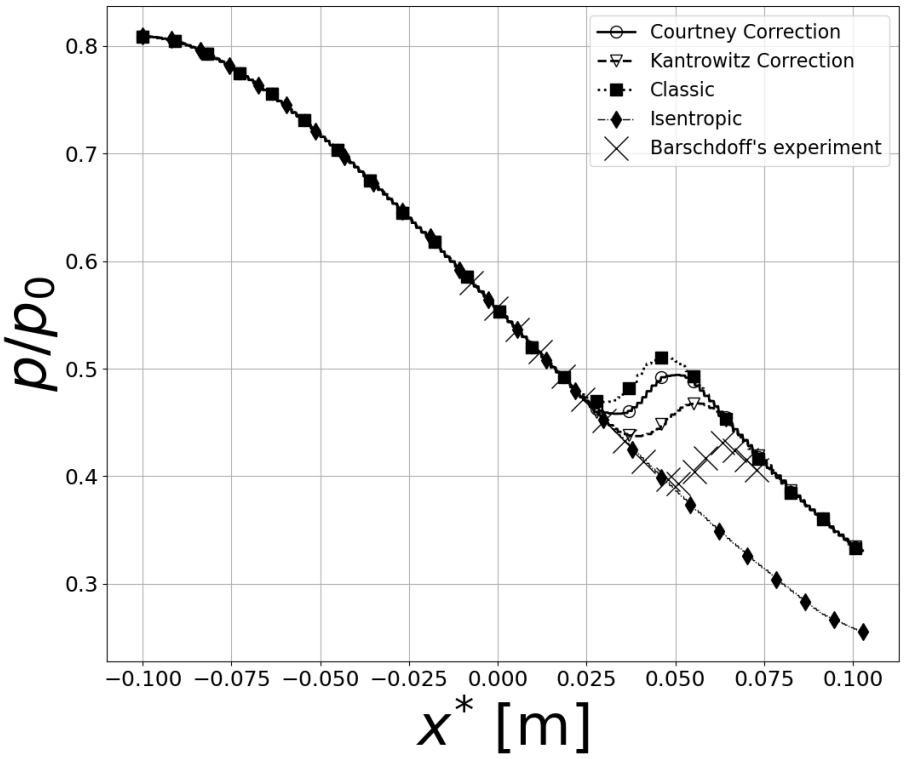

Figure 5.13: Pressure by stagnation pressure ratio comparison for the nucleation models

heat coefficient. Slightly changes in the polynomial fit done with data from NIST base resulted in significant changes in results [30]. Another point to be considered is that we are assuming a perfect gas equation of state, which may not apply; future works could consider the use of a real-gas equation of state, such as Peng-Robinson. Changing the pressure at which the specific heat coefficient is calculated also impacts the onset of condensation, as graphic 5.14 below shows for Courtney's correction. It can be seen that, now, the model captures the onset of condensation, showing that it is very sensitive to changes in the thermophysical properties. Figure 5.15 shows the comparison for the temperature field. As seen in Moore's nozzle, the onset of the condensation happens at higher temperatures for the classic models, followed by Courtney's correction and then Kantrowitz's correction. However, all of them stabilize at the same temperature at the exit of the nozzle. Compared to the isentropic case temperature, an increase of nearly 60 degrees was observed; the energy liberated by the condensation of the steam is responsible for that. All of these results show that as far as we get from the perfect gas assumption, with higher pressures and temperatures, the condensation onset is highly affected, failing

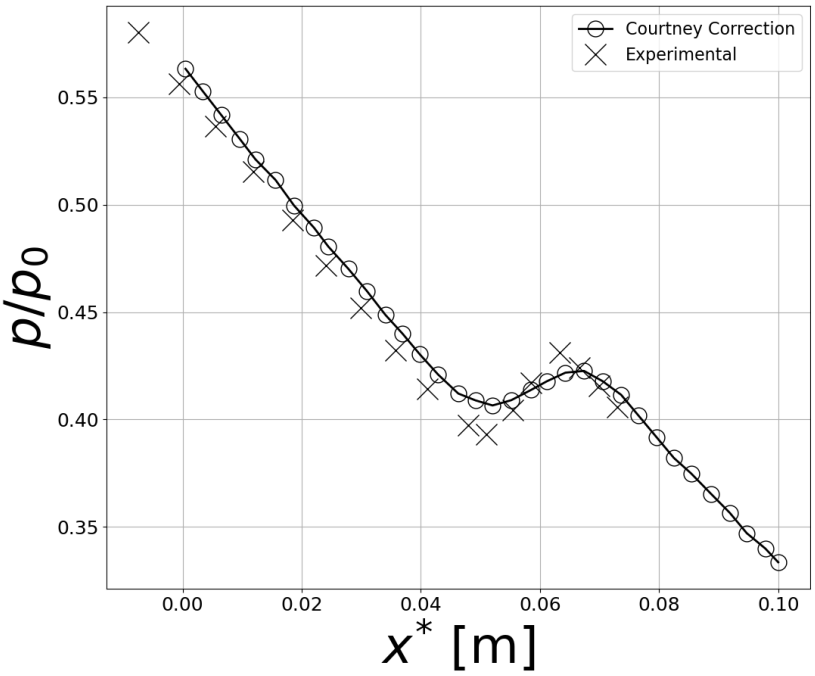

Figure 5.14: Test case with Cp evaluated at saturation pressure.

to capture the exact location of its start; so, an accurate definition of the thermophysical properties and a proper equation of state shows to be of great importance. Figure 5.16

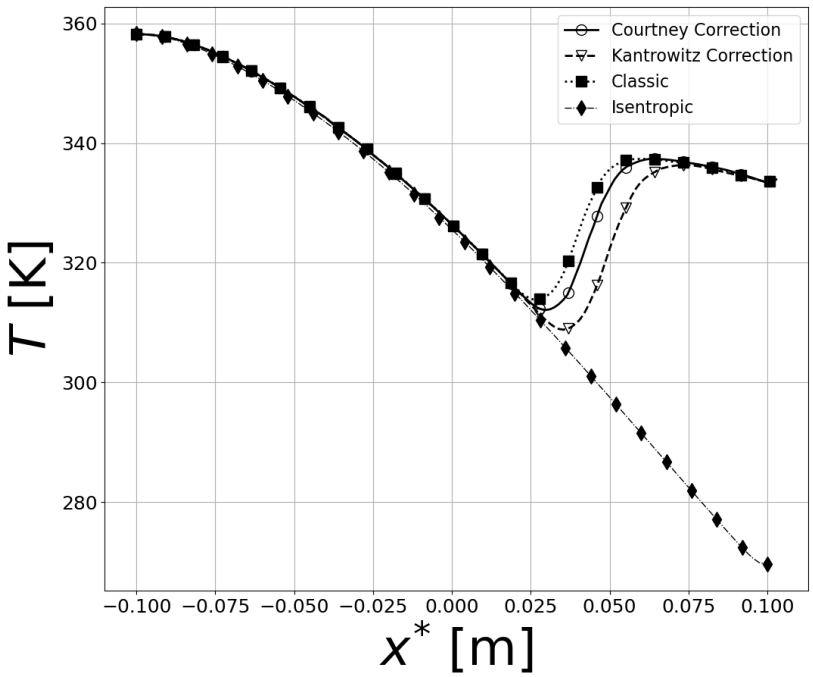

Figure 5.15: Temperature distribution at the center line of the nozzle.

shows the temperature field inside the supersonic nozzle for Kantrowitz's correction model. The qualitative result is basically the same for all three models, so only one model was chosen to represent the fields. In that way, figure 5.17 represents the nucleation and the

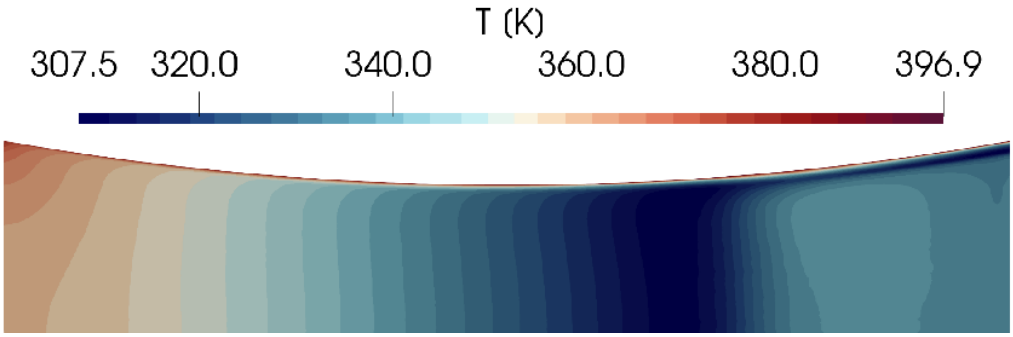

Figure 5.16: Temperature field inside Barschdoff's nozzle.

mass transfer rate fields for Kantrowitz's correction, and it is possible to see that the nucleation stays focused in the area near the throat of the equipment, as expected. Figure

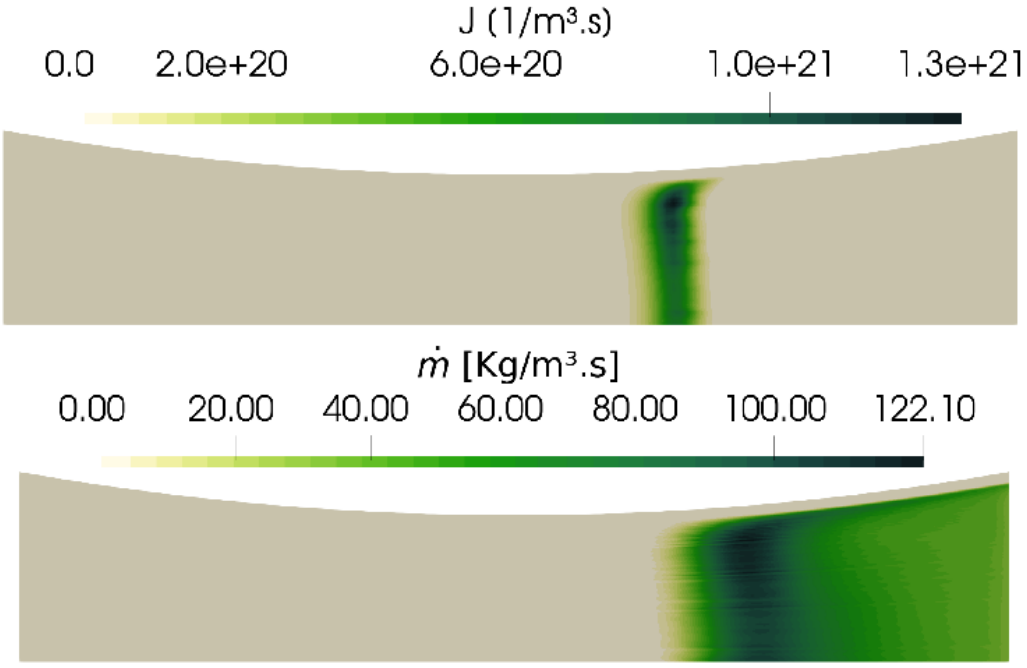

Figure 5.17: Nucleation and mass transfer rates.

5.18 shows the supersaturation degree inside the nozzle, which has a peak value of 6.1, which is less than the achieved in Moore's nozzle (10.5). As for the liquid mass fraction generated, the figure also shows how the condensed steam is distributed along the nozzle. This field is interesting to observe because, in a supersonic separator application, it would be possible to analyze the distribution of liquid inside the equipment and predict ways to

optimize it in a way to direct the condensed particles to the walls and furthermore to the separation chamber.

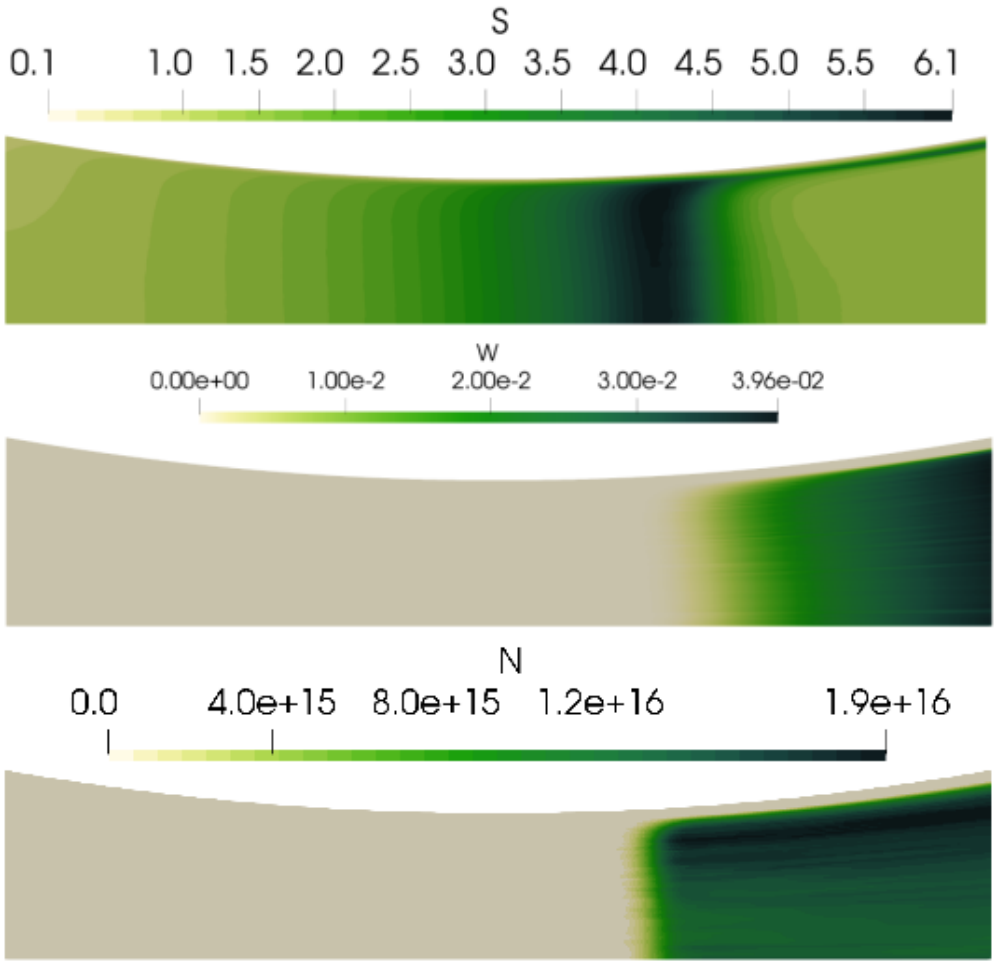

Figure 5.18: Supersaturation degree, liquid mass fraction and number of particles generated fields.

5.2 Supersonic Separator

Finally, in this section, the results of the simulation of a supersonic separator model will be presented and discussed. Since the model was first validated against experimental data and results showed satisfactory qualitative and quantitative agreement with it, it is possible to simulate the performance of the equipment under real work pressure and temperature conditions. Kantrowitz's correction model was the chosen one for this application because it achieved better results in the experimental comparison. Figure 5.19 shows the entire domain of the supersonic separator (clear blue) and the simulated periodic fraction in red. Figure 5.20 shows the slice made into the geometry during the post-processing of

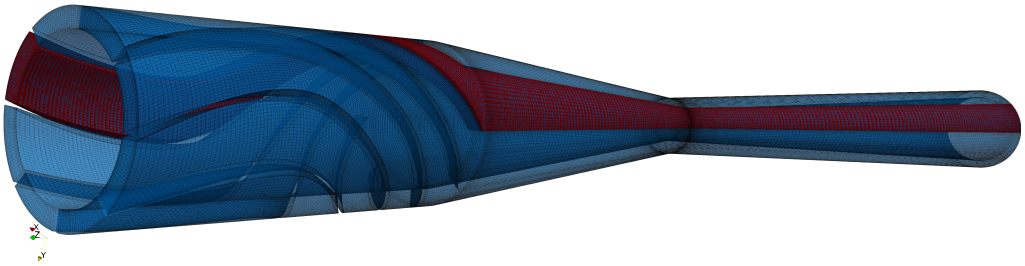

Figure 5.19: Periodic domain of the supersonic separator.

results. Measures of pressure and temperature were taken at the divergent section of the equipment. All of the post-processing was done in ParaView. Figures 5.21, 5.22, and others are related to the slice made in the periodic geometry.

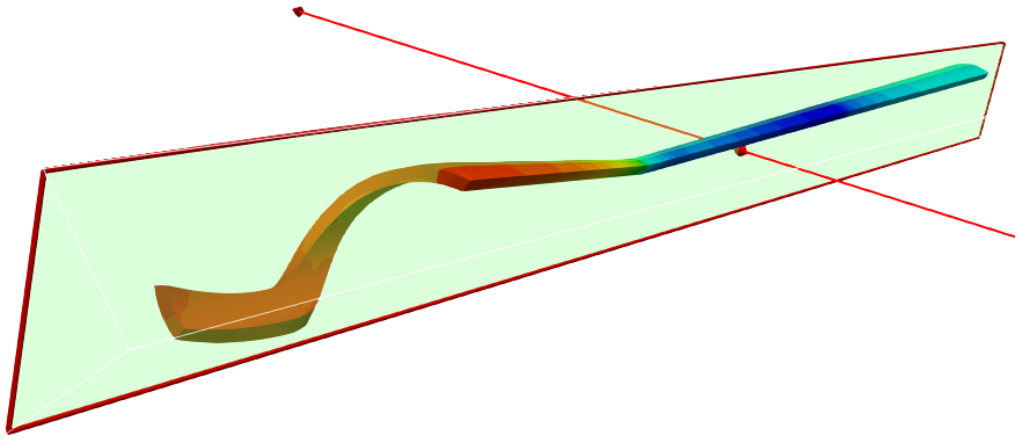

Figure 5.20: Plane used to slice the geometry.

It's possible to see that the temperature suffers a huge drop when it passes through

the throat and the flow accelerates; the minimum temperature reached was 161.6 [K]. After the diverging section, with the pressure recovering, the temperature also rises up to a maximum of 278.5 [K], which is expected for this equipment.

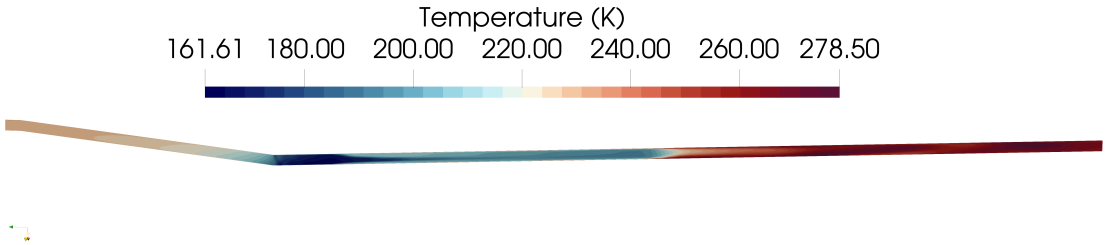

Figure 5.21: Temperature field in the cross-section area.

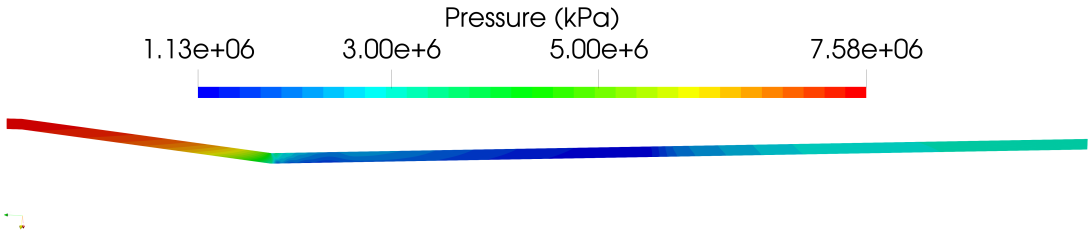

Figure 5.22: Pressure field in the cross-section area.

Figure 5.23 below shows the temperature and pressure distributions along the converging and diverging sections of the equipment, where is possible to see the point of onset of the condensation. The temperature profile seems to be more unstable than the one observed in the supersonic nozzles, which had a smoother, smaller, and more controlled geometry compared to the supersonic separator; besides, the CH4-CO2 mixture is more suitable to such instabilities than the pure steam. The Δp inside the supersonic separator reaches 6.45×10^6 [Pa], with a minimum pressure of 1.13×10^6 [Pa] at 0.11 [m] from the throat. Figure 5.22 shows the pressure distribution along the cross-section area. The pressure gradient increases as the flow reach the nearest section of the supersonic separator and there is the region where shock waves could happen. As this geometry does not have a smooth transition, the simulation captured some fluctuations in the pressure field that can be attributed to the shock or expansion wave formation, but not a rough one. Figure 5.24 below shows in detail the temperature and pressure field in the throat area. Figure 5.25 shows the velocity field in the cross-section area. A maximum velocity of 440 [m/s] was reached in this section, but a maximum velocity of more than 550 [m/s] was reached in the domain, generating a G force equal to 710000. Figures 5.26 and 5.27 refer to the

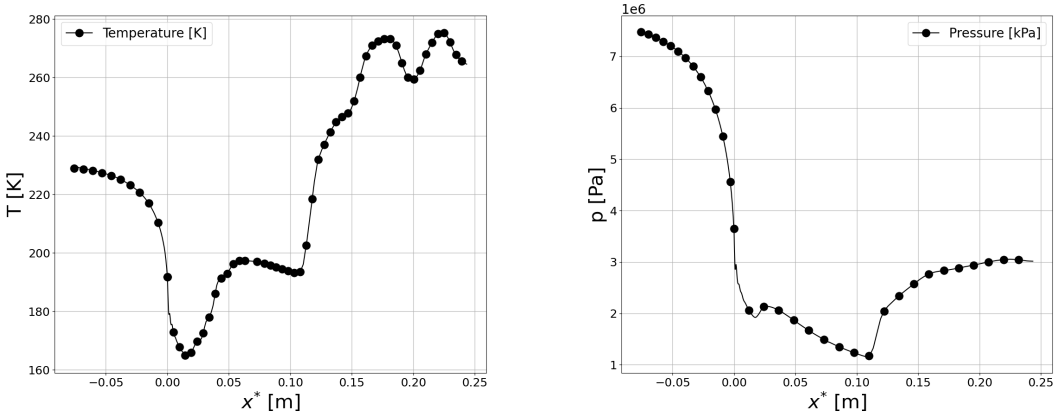

(a) Temperature distribution.

(b) Pressure distribution.

Figure 5.23: Temperature and pressure distributions in the supersonic separator cross-section area.

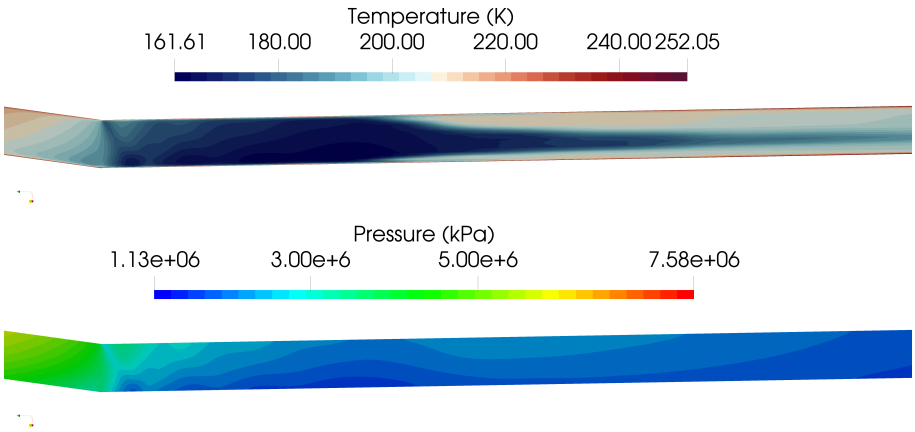

Figure 5.24: Temperature and pressure field detailed.

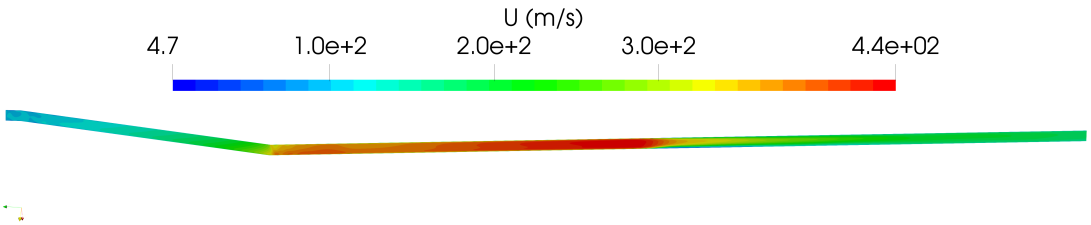

Figure 5.25: Velocity field in the supersonic separator cross-sectional area.

supersaturation degree and nucleation rate near the throat region and the liquid mass fraction generated in the divergent section of the supersonic separator.

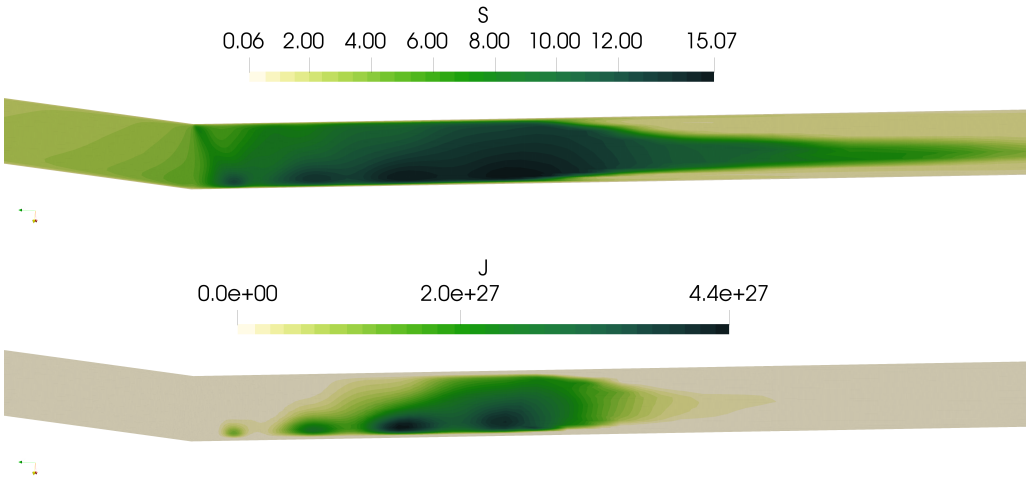

Figure 5.26: Supersaturation degree and nucleation rate fields in the supersonic separator cross-sectional area.

13% of the total 40% of the CO2

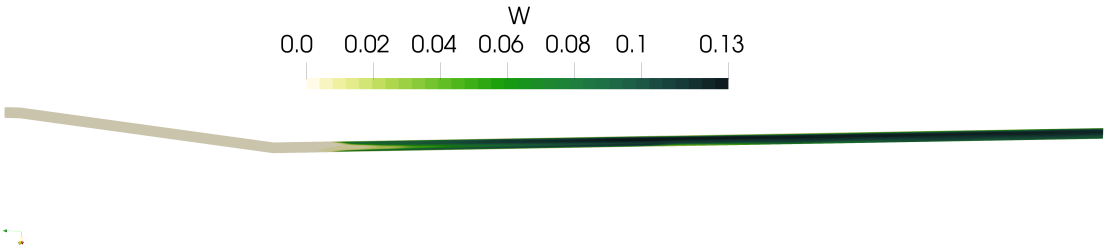

Figure 5.27: Liquid mass fraction field in the supersonic separator cross-sectional area.

Chapter 6

Conclusions

Throughout the study, several models were reviewed and studied with the purpose of using state-of-the-art modeling, where the works of various authors were evaluated. The approach via source term modeling proved to be direct and easier to implement, where a two-component mixture is considered. The classic nucleation modeling studied showed to be still in development, as there is no consensus among authors about which correction of the model to be used, there being a need to adapt some factors to experimental data. Furthermore, the thermophysical modeling of the mixture proved to be a great challenge due to the difficulty of accessing data for certain components of the mixture and for the required operating conditions.

At the end of the work, the computational modeling based on the mathematical modeling of the homogeneous condensation of a component of a compressible, transient, and temperature-varying gaseous mixture was implemented in the OpenFOAM environment, validated, and applied to a supersonic separator under real operating conditions. The solver proved to be functional and capable of capturing the carbon dioxide gas condensation in a mixture with methane gas, which is very promising for industrial applications where it is desired to evaluate the distribution of mixtures within equipment and whether one component will condense or not, with applications in the Oil & Gas and aerospace industries, for example.

Chapter 7

Future works suggestions

One aspect that showed to be very important in the results, is that the model is very sensitive to changes in the specific heat variation curve, for example. The use of an equation of state for a real gas is also an improvement that should be taken into account for future works, as the real operating conditions of a supersonic separator are far from the hypothesis of a real gas. So, as suggestions for future works:

- Improve the thermodynamic characterization of the mixture;
- Apply a real-gas equation of state;
- Study the impact of different turbulence modeling;
- Implementation and verification of the trace component neglected in the modeling of the stress tensor;
- Improve the current code structure for the new nucleation models added.

Bibliography

[1] TACCONI, Z., *Feasibility analysis of a two-fluid solver for cavitation and interface capturing as implemented in OpenFOAM*, Ph.D. Thesis, Politecnico de Milano, 2018.

[2] BAKHTAR, F., YOUNG, J. B., WHITE, A. J., et al., "Classical Nucleation Theory and Its Application to Condensing Steam Flow Calculations". In: *Proceedings of the Institution of Mechanical Engineers*, 2005.

[3] BARSCHDOFF, D., "Verlauf der zustandsgröSSen und gasdynamische zusammenhänge bei der spontannen kondensation reinen wasserdampfes in lavaldüsen", *Forschung im Ingenieurwesen*, 1971.

[4] DING, H., SUN, C., WANG, C., et al., "Prediction of dehydration performance of supersonic separator based on a multi-fluid model with heterogeneous condensation", *Applied Thermal Engineering*, v. 171, pp. 115074, 2020.

[5] WEN, C., KARVOUNIS, N., WALTHER, J. H., et al., "An efficient approach to separate CO2 using supersonic flows for carbon capture and storage", *Applied Energy*, v. 238, pp. 311–319, 2019.

[6] HAHIGHI, M., HAWBOLDT, K. A., ABDI, M. A., "Supersonic separators: Review of latest developments", *Journal of Natural Gas Science and Engineering*, v. 27, pp. 109–121, 2015.

[7] PRAST, H., DAM, R. V., WILLEMS, J. F. H., et al., "Formation of nano-sized water droplets in a supersonic expansion flow", *Journal of Aerosol Science*, v. 27, pp. S147–S148, 1996.

[8] OKIMOTO, F. T., SIBANI, S., LANDER, M., "Twister supersonic gas conditioning process". In: *Abu Dhabi International Petroelum Exhibition and Conference, , Abu Dhabi, Arábia Saudita*, 2000.

[9] SCHINKELSHOEK, P., EPSOM, H. D., "Supersonic gas conditioning low pressure drop twister for NGL recovery". In: *Offshore Technology Conference, Texas, EUA*, 2006.

[10] ALFEROV, V. I., BAGUIROV, L. A., FEYGIN, V. I., et al., "Method of and apparatus for the separation of components of gas mixtures and liquefaction of a gas", *US Patent 6,372,019*, 1999.

[11] ANDERSON, J. D., *Fundamentals of Aerodynamics*. McGraw-Hill Higher Education, 2001.

[12] MAMORU ISHII, T. H., *Thermo-Fluid Dynamics of Two-Phase Flow*. Springer, 2011.

[13] ROSA, E. S., *Escoamento Multifásico Isotérmico - Modelos de Multifluidos e de Mistura*. Artmed Editora, 2012.

[14] MARSCHALL, H., *Towards the Numerical Simulation of Multi-Scale Two-Phase Flows*, Ph.D. Thesis, Technische Universität München, 2011.

[15] ISHII, M., "Drift Flux Model and Derivation of Kinematic Constitutive Laws". In: *Two-phase flows and heat trasnfer: proceedings of NATO Adanced Study Institute*, 1977.

[16] EDATHOL, J., BREZGIN, D., ARONSON, K., et al., "Prediction of non-equilibrium homogeneous condensation in supersonic nozzle flows using Eulerian-Eulerian models", *International Journal of Heat and Mass Transfer*, v. 152, 2020.

[17] RICHARD, B., WERNER, D., "Kinetische Behandlung der Keimbildung in übersättigten Dämpfen", *Annalen der Physik*, v. 416, pp. 719–752, 1935.

[18] MCDONALD, J. E., "Homogeneous nucleation of vapour condensation." *American Journal of Physics*, v. 30, pp. 870–877, 1962.

[19] ABRAHAM, F. F., "Homogeneous nucleation theory", *Academic press, New York*, 1974.

[20] COURTNEY, W. G., "Remarks on homogeneous nucleation", *Journal of Chemical Physics*, v. 35, pp. 2249–2250, 1961.

[21] KANTROWITZ, A., "Nucleation in very rapid vapour expansions", *Journal of Chemical Physics*, v. 19, pp. 1097–1100, 1951.

[22] FEDER, J., RUSSEL, K. C., LOTHE, J., et al., "Homogeneous nucleation and growth of droplets in vapours", *Adv. Physics*, v. 15, pp. 111–178, 1966.

[23] YOUNG, J., "The spontaneous condensation of steam in supersonic nozzle", *Physico Chem Hydrodyn*, v. 3, pp. 57–82, 1982.

[24] POPE, S. B., *Turbulent flows*. Cambridge University Press.

[25] SILVEIRA NETO, A., *Escoamentos turbulentos Análise Física e Modelagem teórica*. Composer.

[26] SILVA FREIRA, A. P., MENUT, P. P. M., SU, J., *Turbulência*. ABCM.

[27] MENTER, F. R., "Two-Equation eddy-viscosity turbulence models for engineering applications", *AIAA Journal*, v. 32, 1994.

[28] OPENFOAM, *OpenFOAM - The Open Source CFD Toolbox - User Guide*, OpenFOAM Foundation, 2nd ed., Feb. 2014.

[29] ALAHMADI, Y. H., NOWAKOWSKI, A. F., "Modified shear stress transport model with curvature correction for the prediction of swirling flow in a cyclone separator", *Chemical Engineering Science*, v. 147, pp. 150–165, 2016.

[30] "Carbon dioxide-Antoine Equation Parameters", Available at: shorturl.at/noDEN, Access 12/11/2021.

[31] STULL, D. R., "Vapor Pressure of Pure Substances. Organic and Inorganic Compounds", *Ind. Eng. Chem.*, v. 39, pp. 517–540, 1947.

[32] SUTHERLAND, W., "The viscosity of gases and molecular force", *Philosophical Magazine*, v. 36, pp. 507–531, 1893.

[33] "NIST-JANAF Thermochemicals Tables", Disponível em: https://janaf.nist.gov/.

[34] "Predicting the fog-drop size in wet-steam turbines", .

[35] MEDRONO, R. E. A., *Desenvolvimento de tecnologia de separação de CO2 do gás natural em velocidades supersônicas.*, Tech. rep., 2021.

[36] W. MALALASEKERA, H. V., *An Introduction to Computational Fluid Dynamics: The Finite Volume Method*. Pearson, 2007.

[37] FERZIGER, J., P. M., *Computational methods for fluid dynamics*. Springer Verlag. [S.l.]: Berlin-New York, 1995.

[38] MOUKALLED, F. H., MANGANI, L., DARWISH, M., *The finite volume method in computational fluid dynamics: an advanced introduction with OpenFOAM® and Matlab®*. Springer, 2016.

[39] OPENCFD, "OpenFOAM. The open source CFD toolbox", 2019.

[40] SPALDING, D. B., "The New "Log of Law"", *Journal of Applied Mechanics, ASME*, pp. 455–457, 1961.

[41] LAUNDER, B. E., SPALDING, D. B., *Mathematical Models of Turbulence*. Academic Press: London, United Kingdon, 1997.

[42] "Salome website", `https://www.salome-platform.org/`, note = Accessed: 2022-10-13.

[43] DE AZEVEDO, P., MORAES, A., SÁ, N., et al., "Viabilidade de geometria periódica para simulação CFD da condensação de CO2 em separadores supersônicos." 2022, Accessed: 2022-10-23.

[44] RUSCHE, H., *Computational Fluid Dynamics Of Dispersed Two-Phase Flows At High Phase Fractions*, Ph.D. Thesis, Imperial College, 2002.

[45] WELLER, H., *Derivation, modelling and solution of the conditionally averaged two-phase flow equations.*, Tech. rep., 2005.

[46] PATANKAR, S., "Numerical heat transfer and fluid flow", 1981.

[47] JASAK, H., *Error analysis and estimation for the finite volume method with applications to fluid flows*. PhD Thesis, Imperial College, 1996.

[48] OPENCFD, *OpenFOAM: The Open Source CFD Toolkit Programmer's Guide*, OpenCFD Ltd., 2007.

[49] MENTER, F. R., KUNTZ, M., LANGTRY, R., "Ten Years of Industrial Experience with the SST Turbulence Model", *Turbulence, Heat and Mass Transfer*, v. 4, 2003.

[50] HELLSTEN, A., "Some Improvements in Menter's k-omega-SST turbulence model". In: 29^th *AIAA Fluid Dynamics Conference, AIAA-98-2554*, 1998.